

## Chapter Ten

# Chalcogenide Glass Thin Film and Fiber Structures for Chemical and Biological Sensing

J. David Musgraves, Sylvain Danto, Kathleen Richardson  
*School of Materials Science and Engineering, Clemson University, Surrine Hall  
Clemson, South Carolina, 29631, USA  
jdm047@clemson.edu*

Juejun Hu  
*Department of Materials Science and Engineering, University of Delaware, 305 DuPont Hall  
Newark, Delaware, 19716, USA*

### 10.1 INTRODUCTION

Chalcogenide glasses (ChGs) are well known for their high infrared (IR) transparency and amenability to fabrication in fiber and thin film forms, which makes them attractive candidates for mid-IR optical chemical and biological sensors. This chapter describes recent advances in the production of sensing devices from a variety of thin film and fiber structures, highlighting the critical materials parameters needed for achieving low loss, high detectivity operation.

Because the sensitivity of chemical sensors in thin-film and fiber form is typically directly related to some physical characteristic, such as optical path length, which is much higher in these low-dimension structures than that of the associated bulk glass optics, the physical form of the sensor ultimately dictates or influences the required material properties such as optical loss, viscosity, or coefficient of thermal expansion.

Sections 10.2 and 10.3 will review the functionality of ChGs in thin film and fiber sensing applications, with a focus on how this functionality is impacted by the choice of ChG constituents. The strengths and drawbacks of these sensing approaches will be discussed, as some ChG compositions are well-known for limited chemical and temperature stability, as well as high photosensitivity, which can make them excellent candidate material systems for use in some sensing regimes and environments, but preclude their use in other applications.

Having outlined the required material characteristics necessary for these sensing applications, the discussion in Section 10.4 will then turn to compositional design approaches used to obtain these characteristics using multi-component ChGs. Varying elemental compositions can be used to tailor glass optical and thermal properties to meet design challenges; however these properties are tightly correlated and so the problem becomes one of global, rather than individual, optimization in the parameter space of interest.

This chapter concludes with a brief discussion of the conclusions of the present review, as well as the future directions the authors see this exciting field expanding to include.



## 10.2 THIN FILM SENSORS

### 10.2.1 *Introduction*

As the planar counterpart of fiber optic sensors, integrated optical sensors use on-chip components such as waveguides and resonators to perform molecular detection. Compared to conventional sensors based on bench-top instruments, integrated planar sensors feature small footprint and low-power consumption, require minimal amount of analyte, and their manufacturing is potentially compatible with standard semiconductor microfabrication process flow [1-3]. ChGs are uniquely poised as an attractive material candidate for on-chip optical sensors: these glasses possess high refractive indices (typically  $n = 2-3$ ), which enable strong optical confinement and compact on-chip integration, their amorphous structure facilitates monolithic planar integration on different substrates, and their broad IR transparency window overlaps with the spectral fingerprints of most chemical and biological species.

These advantages of chalcogenide materials were well recognized even in the very early days of glass waveguide development [4]. Integrated ChG waveguides were first demonstrated in the 1970s on  $\text{LiNbO}_3$  substrates. Spectroscopic sensing applications of planar ChG waveguide devices, although remained unexplored until the last decade, are rapidly becoming a field of intensive scientific investigation in recent years [5], largely spurred by the rapid progress of mid-IR laser sources (quantum cascade lasers [6-8] and interband cascade lasers [9, 10]), uncooled detectors [11], and mid-IR optical fibers [12].

In this section, we will cover the latest developments in the field of planar ChG optical sensors. We will first briefly review device processing and integration techniques for planar chalcogenide sensor fabrication, and then devote the majority of this section to the discussion of molecular detection mechanisms utilized by planar optical sensors. ChGs are also widely applied in electrochemical sensors as the ion-exchange electrode material [13-15]; however, in this section we are limiting our scope to optical sensors.

### 10.2.2 *Planar chalcogenide glass sensor device fabrication and integration*

#### 10.2.2.1 *Micro-fabrication of chalcogenide glass optical sensors*

Planar waveguides, the photonic wires for optical signal transmission on-chip, constitute the basic building block for the vast majority of planar optical sensing systems [16]. Examples of commonly used waveguide-based sensor devices include micro-resonators, interferometers, and waveguide gratings.

#### *Photosensitive patterning of waveguide devices*

This method takes advantage of the well-known photosensitivity in ChGs for nanopatterning: when these glasses are illuminated with light with photon energy close to their band gap, the photo-induced glass network structure relaxation leads to refractive index modification [17]. The photo-induced index increase was employed in planar waveguide sensor fabrication to create channel waveguides in Ge-Sb-Se glass films by selective exposure in the core region [18]. Mid-IR waveguide operating at 8.4  $\mu\text{m}$  wavelength was fabricated using a similar approach with a low optical loss of 0.5 dB/cm [19].

Since the photo-induced index modification is limited in magnitude ( $\Delta n < 0.1$ ), the photosensitive patterning technique generates waveguides with low-index-contrast. The low index

contrast minimizes scattering loss and improves the fabrication tolerance. On the other hand, this relatively low index contrast limits the minimum bending radius of waveguides to a few millimeters. Therefore, alternative designs offering higher index contrast need to be pursued if waveguide sensor designs were to incorporate compact curved sections such as spiral structures.

#### High-index-contrast waveguide fabrication

Most standard microfabrication techniques have been applied to high-index-contrast ChG waveguide processing. In a standard photolithographic process, ultraviolet (UV) lithography is first used to define the desired device patterns in photoresist, and the subsequent pattern transfer to the ChG layer can be executed using wet chemical etching [20, 21], plasma dry etching [22-24], or lift-off [25]. Waveguides with sub-micron core dimensions and low optical losses ( $<1$  dB/cm) have been fabricated using these methods [26]. Fig. 10.1a and 10.1b compare the morphology of waveguides fabricated by dry and wet etching methods; the anisotropic wet etching results in undercut in the glass layer that may compromise precise feature size definition. Therefore dry etching or lift-off are preferred pattern transfer methods for sub-micron single-mode waveguide devices. Other pattern generation techniques alternative to photolithography such as electron beam lithography [27-29] and focused ion beam milling [30, 31] were also explored for ChG device processing.

Besides lithographic patterning, the amorphous structure of ChGs enables direct nanoimprint and embossing shaping of glass devices without requiring an extra pattern transfer step [32-34]. Fig. 10.1c schematically shows the experimental setup used for waveguide embossing [35]. The relatively low softening temperature of  $\text{Ge}_{15}\text{As}_{15}\text{Se}_{17}\text{Te}_{53}$  ChG facilitates a low pressing temperature of 200 °C. Han *et al.* further reported that application of a surface coating on waveguides further improves thermal stability of the waveguide core during embossing, and optical loss as low as 0.52 dB/cm was achieved using this method [36].

In addition to vacuum deposition, ChGs are soluble in amine solutions and thus they are amenable to thin film solution processing [37-39]. Soft lithography techniques such as Micro-Molding In Capillaries (MIMIC) and micro-Transfer Molding ( $\mu\text{TM}$ ), originally developed for polymer waveguide processing [40], were successfully applied to generate low-loss planar optical waveguides.

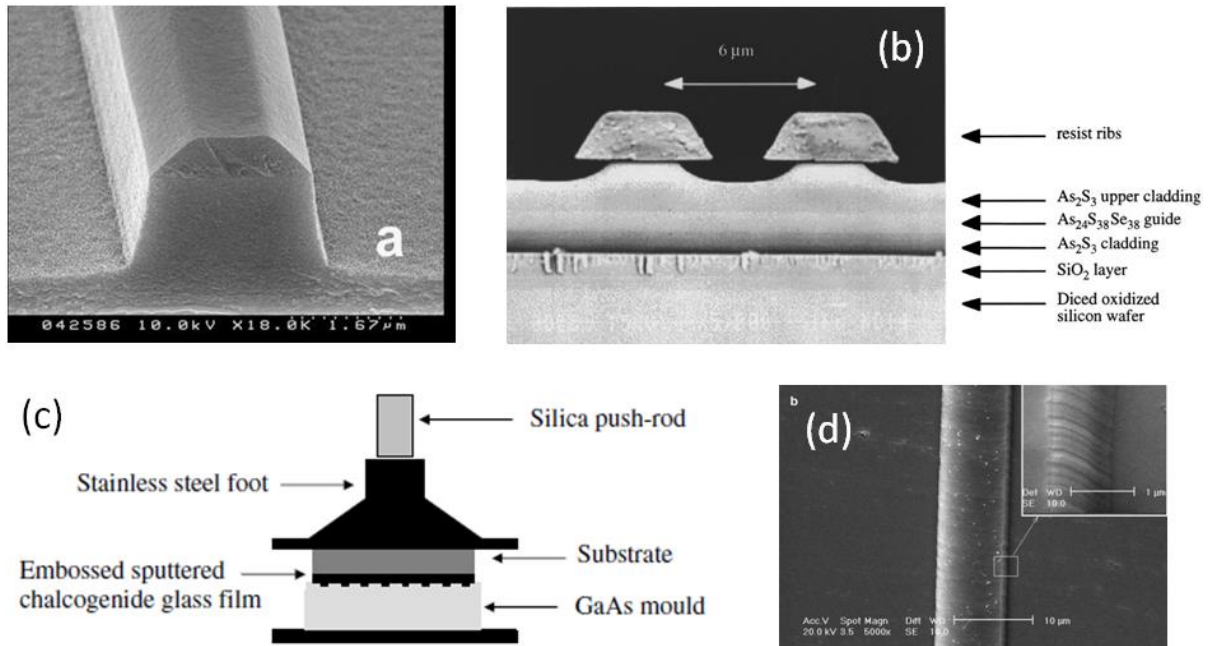


**Fig. 10.1.** (a) SEM image of an  $\text{As}_2\text{S}_3$  waveguides dry etched by inductively coupled plasma (Image courtesy of [23]); (b) Cross-section of a multilayer  $\text{As}_{24}\text{S}_{38}\text{Se}_{38}/\text{As}_2\text{S}_3$  ridge directional coupler; the unstripped resist ridges show the undercutting produced during the  $\text{As}_2\text{S}_3$  glass chemical wet etching using a  $(\text{NH}_4\text{OH})$ -based developer (Image courtesy of [21]); (c) Schematic diagram of the

High-index-contrast waveguides fabricated using the aforementioned techniques often suffer from excessive surface roughness scattering loss, as such scattering loss scales with the square of core-cladding index contrast [41]. As we will see in the detection sensitivity analysis that follows, optical loss is the main sensing performance limiting factor. To mitigate this challenge, thermal reflow was implemented to reduce surface roughness on as-fabricated waveguide devices via the interaction of surface tension [42, 43]. Further optical loss reduction efforts including optimization of the thermal reflow process will be critical to high-sensitivity ChG sensor processing.

#### Hollow-core chalcogenide glass waveguides

Beside traditional index-guiding waveguide devices, hollow-core waveguides using omnidirectional photonic crystals for light confinement are of great interest to sensing, as liquid or gas analyte can be transported in their hollow cores alongside with optical field [44-46]. The large spatial overlap of analyte medium and the optical field promotes photon-molecule interactions for sensitive molecular detection.

DeCorby *et al.* developed a guided self-assembly technique for hollow-core waveguide fabrication based on controlled photodoping in ChGs [47, 48]. The hollow core in their device structure was surrounded by omnidirectional Distributed Bragg Reflector (DBR) mirrors consisting of alternating polyamide-imide (PAI) polymer and  $\text{Ge}_{33}\text{As}_{12}\text{Se}_{55}$  layers (Fig 10.2a). The fabrication process is schematically illustrated in Fig. 10.2b. Silver lines were first patterned using a lift-off method at the intended waveguide location. Upon illumination or heating, photodoping of silver into ChG occurs [49]. The photodoping process is accompanied by an increase of the compressive stress in the layers, which leads to delamination and buckling of the top DBR mirror to form the hollow core waveguide structure. Optical loss as low as 4 dB/cm was reported in the near-IR. A

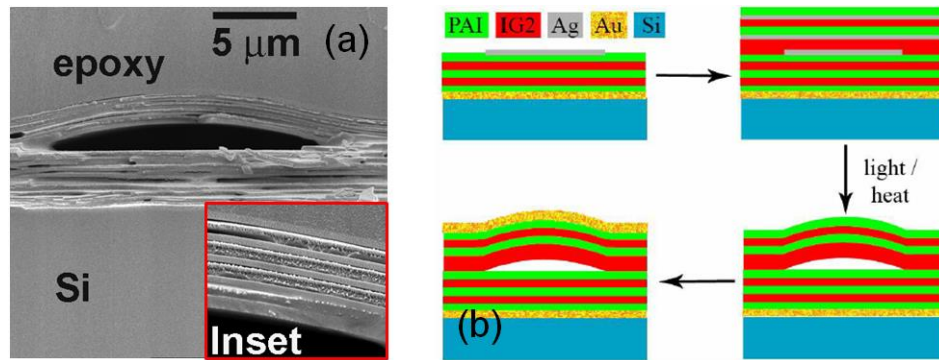


**Fig. 10.2.** (a) SEM image of the cleaved facet of a hollow core waveguide; inset shows high magnification image of the top mirror (Image courtesy of [47]); (b) Schematic fabrication process flow of hollow core ChG waveguides, which is based on controlled film buckling induced by silver photodeposition (Image courtesy of [48]).

chip-scale micro-spectrometer based on out-of-plane modal cut-off in hollow core waveguides was also demonstrated by the team [50, 51].

### 10.2.3 On-chip integration

ChG thin films can be deposited using a variety of vapor and wet chemistry methods on different substrates, and usually at relatively low substrate temperature. This versatility is particularly advantageous for sensor processing, as an on-chip sensing device necessarily involves monolithic or hybrid integration with different functional components such as a light source, a photodetector, and an analyte transport system.

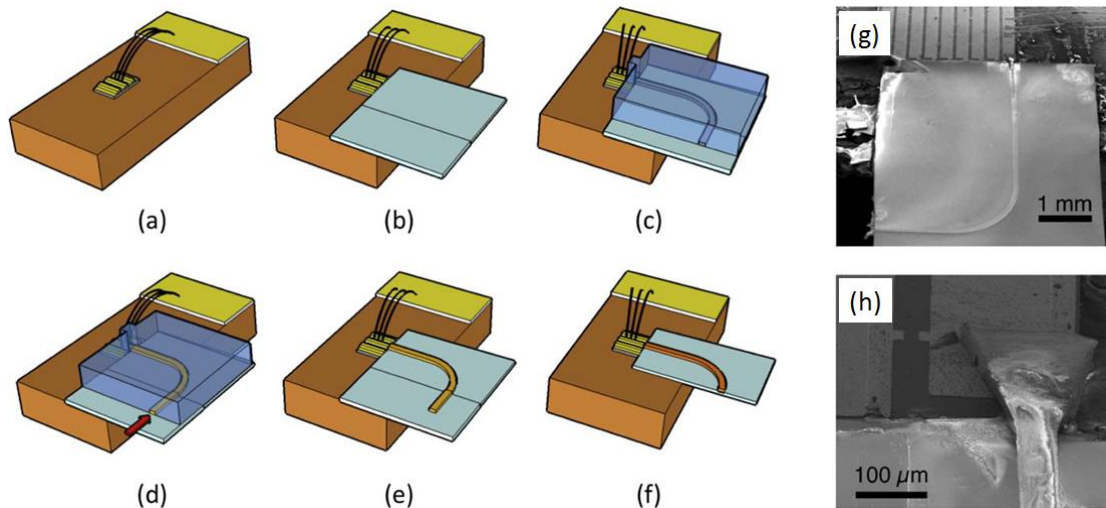


**Fig. 10.3.** ChG waveguide-QCL integration process (a) The QCL chip was soldered onto a Cu heat sink; (b) a 190- $\mu\text{m}$  thick, pre-cleaved glass coverslip was glued onto the Cu block to serve as the waveguide substrate; (c) a polydimethylsiloxane (PDMS) polymer mold attached to the coverslip; (d) amine solution of  $\text{As}_2\text{S}_3$  glass filled the mold by capillary action; (e) the mold was removed after post-baking to solidified the  $\text{As}_2\text{S}_3$  waveguide; (f)

Hybrid integration of solution-processed  $\text{As}_2\text{S}_3$  ChG waveguides with mid-IR Quantum Cascade Lasers (QCL) was recently reported by Tsay *et al.* [52]. Fig. 10.3a-f outlines the integration process flow. The key to the integration process is the use of the additive microfluidic-assisted MIMIC technique, which enables the waveguide formation and alignment in a single step. This proof-of-concept demonstration established an important step towards mid-IR integrated photonics on a chipscale platform for spectroscopic sensing applications. Parallel to the hybrid approach, monolithic integration of chalcogenide devices with lead salt photodetectors was theoretically investigated by Singh *et al.*[53].

## 10.2.4 Planar chalcogenide glass optical sensor detection mechanisms

### 10.2.4.1 Infrared absorption spectroscopy

#### Waveguide evanescent sensors

The majority of ChG planar optical sensors detect molecules by identifying their IR absorption fingerprints. The basic sensing mechanism is similar to that of FEWS (for Fiber Evanescent Wave Spectroscopy): evanescent wave of guided mode in glass waveguides interacts with optically absorbing molecules, leading to attenuation of transmitted intensity at particular wavelength corresponding to the molecular characteristic absorption lines. Fig. 10.4 schematically illustrates the waveguide sensor measurement setup: light from an IR source is coupled into a planar waveguide, and the transmitted intensity is monitored at the waveguide output as a function of wavelength to generate a spectrograph. The absorption line shape and position are used to identify the molecular species, while the absorption line intensity can be used for quantitative measurement of molecular concentration. In one possible configuration, the light source is a broadband halogen lamp or glow bar source, and the spectrograph is obtained by using a spectrophotometer to separate output light at different wavelengths. Alternatively, a tunable IR laser can be used in conjunction with a single-element photodetector to generate the spectrograph using a wavelength-scanning technique [54]. Compared to blackbody broadband sources, tunable lasers typically offer much higher spectral intensity and hence improved detection sensitivity. Mid-IR external cavity quantum cascade lasers are ideal light sources for such applications given their broad spectral tuning range, narrow emission line width, and stable power output [55]. Finally, coupling of light from the source into planar ChG waveguides has been successfully implemented using a variety of schemes, including lens focusing [19, 56], direct butt coupling from laser chips [24], optical fiber end-fire [23, 57], and prism coupling [58].

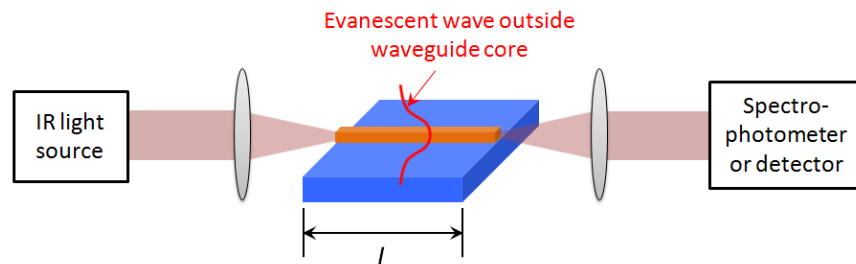


**Fig. 10.4.** Waveguide evanescent wave sensing setup: light from an IR source is coupled into a planar waveguide, where the evanescent wave interacts with molecules leading to optical absorption. The resulting transmitted intensity reduction is detected at the

The two key performance metrics for a sensing technique are specificity and sensitivity. Specificity of IR absorption spectroscopy relies on identification of characteristic absorption lines of target molecules at particular wavelengths. In dilute gaseous medium at room temperature, spectral widths of small molecule absorption peaks due to Doppler broadening are well below  $0.01 \text{ cm}^{-1}$ , and therefore accurate species identification is usually not an issue [59]. Absorption features in liquid analytes or those of macromolecules and biological species, however, are spectrally broad and accurate peak assignment can become a significant challenge. To alleviate this problem, parameter extraction techniques such as Principal Component Analysis (PCA) can be applied to enhance the specificity. As an example, Yang *et al.* demonstrated detection of two types of bacteria, *E. coli* and *S. aureus*, by Attenuated Total Reflection (ATR) measurement using a  $\text{Ge}_{10}\text{As}_{15}\text{Te}_{75}$  ChG ATR plate [60]. The two bacteria strains were clearly distinguished using PCA despite their similar IR spectra.

An alternative approach to improve detection IR biosensing specificity involves chemical functionalization to generate a sensor surface that specifically binds to the target species. Since antibodies bind to their conjugate antigen proteins with good specificity, bio-functionalization is usually accomplished by attaching antibodies to the surface. Functionalization of ChG waveguide surfaces using a gold-thiol chemistry was demonstrated by Yu *et al.* and Anne *et al.* [18, 61, 62]. Fig. 10.5a schematically illustrates the surface functionalized ChG sensor structure. Results from both groups were obtained on Ge-based ChG films deposited on silicon substrates. A thin gold layer with  $\sim 20 \text{ nm}$  thickness was subsequently deposited on top of the glass films, followed by surface anchoring of thiol molecules to form self-assembled monolayers (SAMs) to which antibodies can be attached. The thiol anchor molecule SAMs act as intermediate agents which bind antibodies to the gold surface: their -SH head groups are linked to the gold surface through semi-covalent gold-sulfur bonds, and the SAMs also contain carboxyl or amine groups on the other end for binding with antibodies. Specificity is thus achieved by functionalizing the sensor surface with antibodies that are conjugate to the target biological agents. As an example to showcase surface binding specificity of this functionalization approach, IR spectra of Ge-Sb-Se films functionalized with anti-*E. coli* O157:H7 antibodies were collected using an FTIR microscope in a reflection mode [18]. Fig. 10.5b shows the spectra of the films treated with *E. coli* O157:H7, *E. coli* K12, and *S. enteritidis* suspended in a buffer solution. Distinct IR bands from the film treated with *E. coli* O157:H7 were observed, while the spectrum of the film surface treated with the other two organisms was similar to buffer treated blank films, thus confirming specificity. While the gold-thiol chemistry was validated as an effective surface functionalization method for glass sensors, the introduction of metal gold results in large optical loss. Possible alternative metal-free recipes, for example silane chemistries [63], may be applied to functionalize chalcogenide sensors with a thin silicon dioxide surface coating with minimal parasitic optical loss.

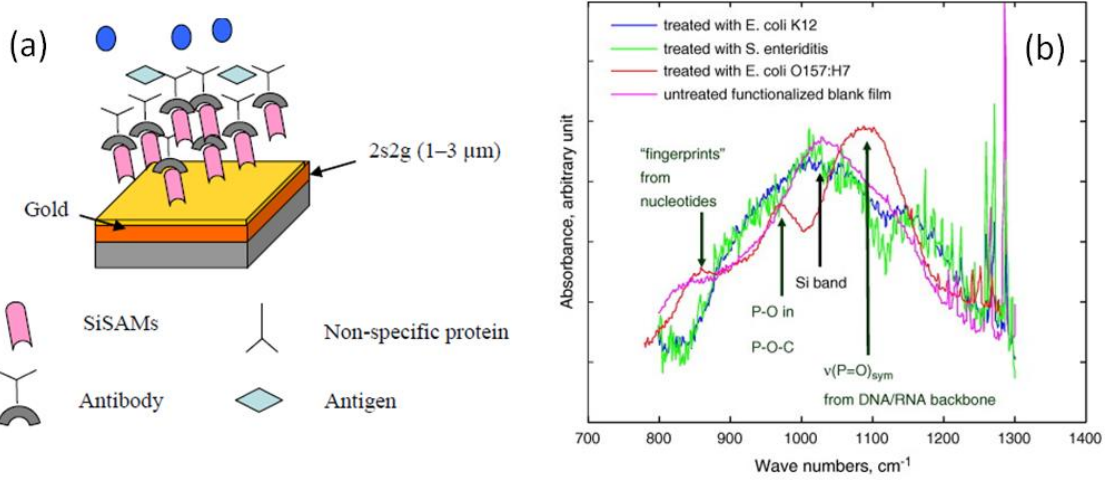


**Fig. 10.5. (a)** Schematic of a chalcogenide thin film sensor structure whose surface is functionalized using a gold-thiol chemistry for selective binding with biological agents (Image courtesy of [61]); **(b)** Mid-IR spectra of anti-*E. coli* O157:H7 antibody functionalized  $\text{Co}_2\text{S}_3$ - $\text{Sb}_2\text{S}_3$

Sensitivity of waveguide evanescent wave sensors can be conveniently analyzed using the Lambert-Beer's Law. The intensity reduction  $\Delta I$  due to target molecule absorption through a waveguide section of length  $L$  is given by:

$$\Delta I = I_0 \cdot \left| 1 - \exp(-\Gamma \alpha L) \right| \quad (10.1)$$

where  $I_0$  is the optical intensity measured at the waveguide output when no absorbing molecular species is present (i.e. the blanket reference),  $\alpha$  is the attenuation coefficient of the analyte, and  $\Gamma$  represents the optical confinement factor in the evanescent wave, which is given by [64]:

$$\Gamma = \frac{nc_0 \varepsilon_0 \iint_{ev} |E|^2 dx dy}{\iint_{\infty} \text{Re}(E \times H^*) \cdot \hat{z} \cdot dx dy} \quad (10.2)$$

Here  $n$  is the refractive index of the medium,  $c_0$  is the light velocity in vacuum,  $\varepsilon_0$  denotes the vacuum permittivity, and  $E$  and  $H$  are the waveguide mode electric and magnetic fields. The integral in the numerator is carried out only in the evanescent wave domain. Clearly different orders of waveguide modes lead to different confinement  $\Gamma$ ; thus to ensure measurement reproducibility, single mode waveguide is strongly preferred over multi-mode waveguides for spectroscopic sensing applications.

Sensitive detection of trace amount of target molecules with small  $\alpha$  requires optimized sensor designs to maximize  $\Delta I$ . As is seen from the two equations, such optimized design should come with large  $\Gamma$  and  $L$ ; in other words, both optical confinement and interaction length should be large to enhance the interaction strength between light and molecules. Optical confinement in the evanescent wave is increased by shrinking at least one linear dimension of the waveguide to a sub wavelength-scale. The interaction length  $L$  is ultimately limited by intrinsic optical attenuation in the waveguide. As a rule of thumb, if we denote the intrinsic waveguide modal attenuation coefficient as  $\alpha_{wg}$  (in  $\text{cm}^{-1}$ ), the optical path length  $L$  is of the order of  $1/\alpha_{wg}$ . Planar single-mode high-index-contrast waveguides fabricated using state-of-the-art technologies can reach a low optical loss value down to 0.03 dB/cm in silicon nitride waveguides [65].  $\text{As}_2\text{S}_3$  ChG waveguides with a low propagation loss of 0.05 dB/cm was also reported by Madden *et al.* [66]. The optical path length

accessible to waveguide sensors is thus roughly a few tenths of centimeters. Such a long waveguide section can be compactly laid out on a chip-scale device in serpentine [66] or spiral patterns [67, 68] to conserve real estate on-chip.

On-chip analyte transport can be realized by integrating microfluidic flow systems or miniaturized gas chambers with the sensor device [69]. Hu *et al.* demonstrated a microfluidic sensor device monolithically integrated with planar Ge-Sb-S ChG waveguides [70]. Quantitative chemical sensing via evanescent wave absorption spectroscopy was demonstrated using the microfluidic device.

### Cavity-enhanced absorption spectroscopy

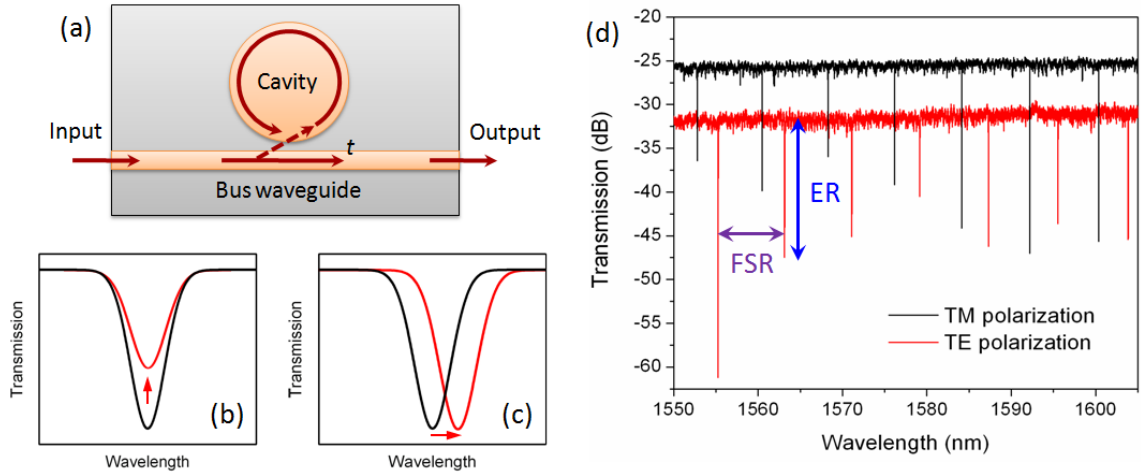


**Fig. 10.6. (a)** Schematic top-view of a resonator sensor device, consisting of a micro-disk cavity and a bus waveguide side-coupled to the cavity for optical input/output; the bottom figures illustrate the device transmission spectra correspond to two different sensing modes **(b)** absorption spectroscopy and **(c)** refractometry; **(d)** transmission spectra of a 20 μm radius As<sub>2</sub>S<sub>3</sub>

On-chip micro-resonators (micro-cavities) offer an alternative planar sensor design to waveguide evanescent wave devices. Most commonly used micro-resonator geometries include micro-ring/racetrack resonators [72-74], micro-disks [73], and photonic crystal cavities [28, 75, 76]. Fig. 10.6a schematically illustrate the basic structure of a resonator sensor consisting of a micro-disk cavity and a bus waveguide side-coupled to the cavity. Compared to waveguide sensors, resonators boast significantly reduced footprint without compromising detection sensitivity, a highly desirable feature for on-chip integration. This unique advantage is achieved by creating a long effective optical path length through resonance enhancement. Here we use a single-transverse-mode micro-ring/disk in an all-pass configuration (Fig. 10.6a) as an example to illustrate the operating principles of resonator sensors. Transmittance through a resonator can be modeled using the coupling matrix formalism [77] as:

$$T(\lambda) = \frac{|t|^2 + \exp(-\alpha_r L_r) - 2|t| \cdot \exp\left(-\frac{1}{2}\alpha_r L_r\right) \cdot \cos\left(\frac{2\pi n_{eff} L_r}{\lambda}\right)}{1 + |t|^2 \cdot \exp(-\alpha_r L_r) - 2|t| \cdot \exp\left(-\frac{1}{2}\alpha_r L_r\right) \cdot \cos\left(\frac{2\pi n_{eff} L_r}{\lambda}\right)} \quad (10.3)$$

where  $\lambda$  represents the wavelength,  $\alpha_r$  denotes the optical propagation loss in the resonator,  $L_r$  is the resonator perimeter length,  $t$  is the wave amplitude transmission coefficient through the bus waveguide-resonator coupling section, and  $n_{\text{eff}}$  gives the effective index of the resonator. Transmission spectrum given by this equation is characterized by a set of dips occurring at resonant wavelengths  $\lambda = \lambda_r$ :

$$N\lambda_r = n_{\text{eff}}L_r \quad (N \in \mathbb{Z}^+) \quad (10.4)$$

that is, when the integral multiples of wavelength equals the resonator perimeter, light coupled from the bus waveguide to the cavity can circulate inside the resonator and interfere constructively at each round-trip to create a folded, long effective optical path length. If the refractive index of the surrounding medium is modified due to molecular binding on the resonator surface,  $n_{\text{eff}}$  is changed and the resonance dips shift in wavelength. Such resonance shift can be exploited for sensing in a refractometry mode (Fig. 10.6c), which we will discuss in the next section. The minimum transmittance at resonance  $T(\lambda_r)$  is a function of  $\lambda$  and  $t$ . By setting  $\lambda = \lambda_r$  in Eq. 10.3, we define the resonance Extinction Ratio (ER) in decibel (dB) as:

$$\text{ER} = -10 \cdot \log_{10} [T(\lambda_r)] = -20 \cdot \log_{10} \left[ \frac{|t|^2 - \exp(-0.5\alpha_r L_r)}{1 - |t| \cdot \exp(-0.5\alpha_r L_r)} \right] \quad (10.5)$$

As a consequence, when the propagation loss  $\alpha$  is increased due to evanescent wave interaction with optically absorbing molecules, the extinction ratio is also changed. In resonant cavity-enhanced absorption spectroscopy, optically absorbing molecules are detected by monitoring such extinction ratio change, as is illustrated in Fig. 10.6b [78]. Unlike waveguide sensors, which are inherently broadband devices, both cavity refractometry and absorption spectroscopy techniques operate only at the optical resonance wavelengths. As a result, their wavelength resolution is given by the resonator's Free Spectral Range (FSR), i.e. the wavelength separation between two adjacent resonance dips:

$$\text{FSR} = \frac{\lambda_r^2}{n_g L_r} \quad (10.6)$$

where  $n_g$  is the group index of the resonant mode.

Sensitivity of resonant cavity sensors operating in the absorption spectroscopy mode was both theoretically and experimentally investigated by several groups [78-80]. Effective optical path length  $L_{\text{eff}}$  in a resonant cavity at resonance  $\lambda_r$  can be estimated by the formula:

$$L_{\text{eff}} \sim \frac{1}{\alpha_r} = L_r \cdot \frac{F}{2\pi} \quad (10.7)$$

Here  $F$  is the cavity finesse and the factor  $F/2L_r$  manifests the optical path length enhancement effect with respect to the cavity physical length  $L_r$  at the resonance wavelength. Similar to waveguide evanescent sensors, the sensitivity of resonator sensors is also ultimately bounded by intrinsic propagation loss in the device.

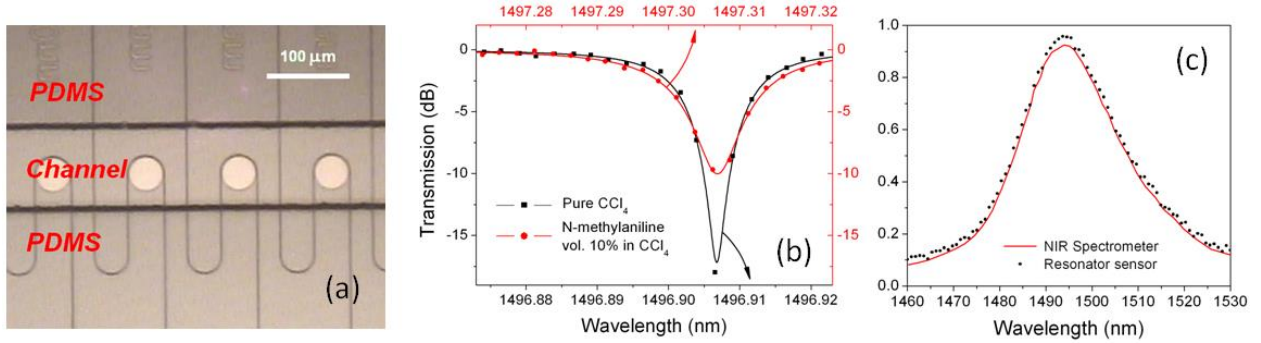


**Fig. 10.7.** (a) Top-view of a PDMS microfluidic channel overlaid with a linear array of Ge-Sb-S microdisks; (b) Microdisk transmission spectra around a resonant peak before and after N-methylaniline solution injection: the dots are experimentally measured data points and the lines are theoretical fitting results; (c) absorption coefficient of N-methylaniline solution measured using the micro-disk cavity

As an illustration of the operating principles of cavity-enhanced absorption spectroscopy, 10.7a shows a top-view micrograph of a planar ChG resonator sensor, which was comprised of a linear array of Ge-Sb-S micro-disk resonators bonded with a PDMS polymer microfluidic channel [79]. To validate the sensing capability of the device, the microfluidic channel was sequentially filled with pure carbon tetrachloride ( $\text{CCl}_4$ ) and 10% volume N-methylaniline solution in  $\text{CCl}_4$ .  $\text{CCl}_4$  is transparent at the near-infrared (NIR) wavelength range while N-methylaniline features an absorption peak centered at around 1496 nm wavelength [81]. As a consequence of the additional absorption loss introduced by the N-methylaniline solution, the resonant dip extinction ratio was decreased (the red curve in Fig. 10.7b). According to Eq. 10. 5, the change of extinction ratio can be used to quantitatively calculate the absorption coefficient of the N-methylaniline solution. Since this approach calculated the analyte absorption only at the resonant wavelengths, the resulting data consist of a set of discrete points spaced by the resonator FSR. Data obtained using this method showed excellent agreement with spectrum measured using a benchtop NIR spectrophotometer (Fig. 10.7c), which confirmed the validity of the cavity-enhanced sensing technique.

### Photothermal detection techniques

Based on our analysis above, the sensitivity of both waveguide evanescent wave sensors and cavity-enhanced absorption spectroscopy was limited by optical propagation loss in on-chip devices. Compared to the well below dB/m-level low optical loss routinely obtained in ChG IR fibers nowadays, planar guided wave devices exhibit much higher loss typically in the dB/cm range. As a consequence, the effective optical path length accessible to planar sensors is of the order of centimeters. When gauged using gas concentration Limit Of Detection (LOD), on-chip IR absorption spectroscopic sensors demonstrated to date claim an LOD value at the parts-per-million (ppm) level [79, 82], much inferior compared to the parts-per-billion (ppb) or even sub-ppb level LOD of free-space cavity-enhanced IR spectroscopic sensors [54, 83, 84] which boast effective optical path lengths of hundreds of meters. Reduced optical loss can be achieved using a large-core rib waveguide design [66] although their small evanescent field component and relatively large bending radius make them not ideal for sensing applications.

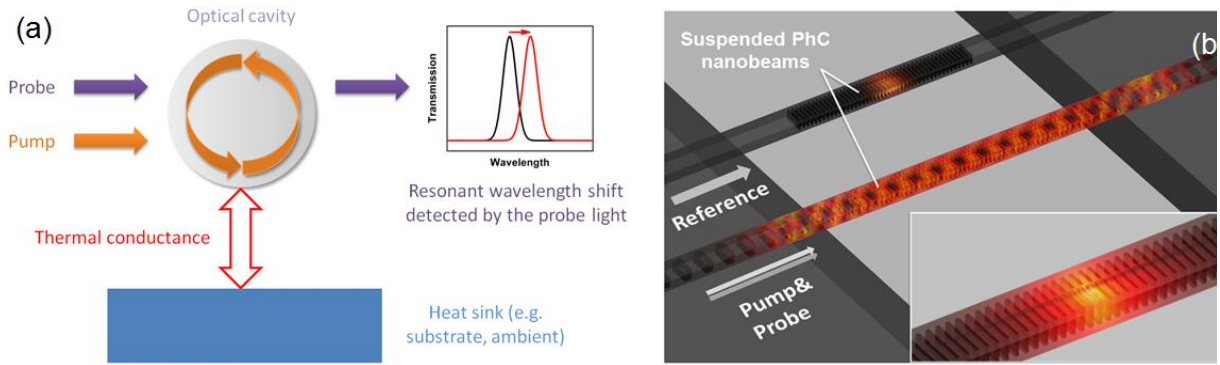


**Fig. 10.8. (a)** Block diagram illustrating the operating principle of nano-cavity photothermal sensing; **(b)** Tilted view of a suspended double resonance PhC nanobeam sensor cavity and a reference cavity. Optical absorption by target analyte molecules at the pump wavelength leads to

We recently proposed and theoretically analyzed an on-chip nano-cavity photothermal sensing technique to overcome this sensitivity bottleneck [85, 86]. The technique works as follows (Fig. 10.8a): a mid-IR pump beam whose wavelength is tuned to match a characteristic absorption line of target molecules is launched into a resonant cavity to induce optical absorption and photothermal effect. Heat generated in the absorption process then leads to temperature rise of the cavity, which induces thermo-optic resonance spectral shift at the probe wavelength. The resonant wavelength shift is subsequently detected using a low-power near-IR probe beam to quantify the target species concentration. This approach has two significant advantages over the methods outlined in previous sections: 1) ultra-high sensitivity is attained by both optical resonance enhancement and thermal confinement; and 2) since mid-IR absorption is translated into photothermal resonance shift at the near-IR probe wavelength, the technique can operate using high performance photodiodes at telecommunication bands rather than resorting to cryogenically cooled mid-IR detectors.

ChGs are uniquely poised for such photothermal sensing applications given their low thermal conductivity and large thermo-optic coefficient. The photothermal Figure Of Merit (FOM) is defined as:

$$FOM = n \cdot \kappa^{-1} \cdot \frac{dn}{dT} \quad (10.8)$$

where  $n$  is the refractive index (optical confinement),  $\kappa$  denotes the thermal conductivity (thermal isolation), and  $dn/dT$  is the thermal-optic coefficient (the ability to convert temperature change to resonance shift). The FOM of ChGs is over 100 times higher than those of silica and silicon. Coupled

with a suspended photonic crystal cavity design to minimize thermal leakage (Fig. 10.8b), our analysis showed that detection down to a single gas molecule is possible using this technique. This detection limit represents four orders of magnitude improvement compared to the LOD of current on-chip IR sensors.

### 10.2.5 **Refractometry sensing**

Refractometry sensing works by detecting refractive index change induced by molecular binding to sensor surfaces. Surface Plasmon Resonance (SPR) is probably the most widely adopted refractometry sensing method [87-90]. Commercial benchtop SPR systems have been well matured in the past three decades [91], and their current applications span from laboratory molecular interaction studies [92] to high throughput screening in the pharmaceutical industry [93]. Unlike IR absorption spectroscopy, which detects molecular species by identifying their characteristic absorption bands, refractometry is inherently non-specific and has to rely on surface receptor coatings which selectively bind to target molecules.

ChG-based SPR detection has recently been evaluated [94-97]. The SPR peak position is extremely sensitive to refractive index variation in the sensing medium caused by presence of molecules, and the technique works by monitoring the SPR dip shift using a Kretschmann angular interrogation geometry. A refractive index detection limit of  $3 \times 10^{-5}$  Refractive Index Unit (RIU) was experimentally demonstrated in the ChG-based SPR sensing system [95].

Refractometry sensing can also be performed using optical resonant cavities by tracking the resonant wavelength shift induced by molecular binding (Fig. 10.6c). Optical resonant cavity sensors operating in the refractometry sensing mode have been realized in a number of material platforms including silica glass [98-100], silicon [69, 101-103], silicon nitride [104], and polymers [105, 106]. ChG resonators with a high loaded quality factor up to  $2 \times 10^5$  were also explored for refractometry sensing applications [107], and a detection limit of  $8 \times 10^{-7}$  RIU was confirmed using bulk refractive index sensing experiments. Giammarco *et al.* applied a polymer enrichment coating on top of Ge-Sb-S glass sensors and demonstrated refractometry sensing of different organic small molecules [108]. Composition and layer structures of the polymer coatings were engineered to achieve selective adsorption affinity to different molecular species.

Besides SPR and resonators, other glass device platforms potentially suitable for refractometry detection include interferometers and waveguide Bragg gratings [109].

### 10.2.6 **Surface Enhanced Raman Spectroscopy (SERS)**

Surface Enhanced Raman Spectroscopy (SERS) is another emerging sensing technique receiving much attention nowadays. Compared to linear optical effects such as absorption and fluorescence, Raman is a nonlinear process with a much smaller scattering cross-section (typically  $10^{14}$  times smaller than fluorescence emission cross-section, for example). In SERS, the weak Raman interaction is dramatically amplified by synergistically combining electromagnetic field enhancement with chemical enhancement effects [111, 112]. High electromagnetic field enhancement is usually attained by excitation of Localized Surface Plasmon Resonance (LSPR) in metallic nanostructures, such as metal nanoparticle dimers and 2-D arrays. To ensure reproducible enhancement, SERS substrates decorated with these metallic nanostructures are usually fabricated using electron beam lithography top-down approach, which is a relatively expensive and slow process [113]. Su *et al.* investigated a new SERS substrate fabrication route using photosensitive patterning of ChGs [114, 115]. Su *et al.* used a two-beam interference lithography system to expose an  $As_2S_3$  film. Photostructural change in the exposed

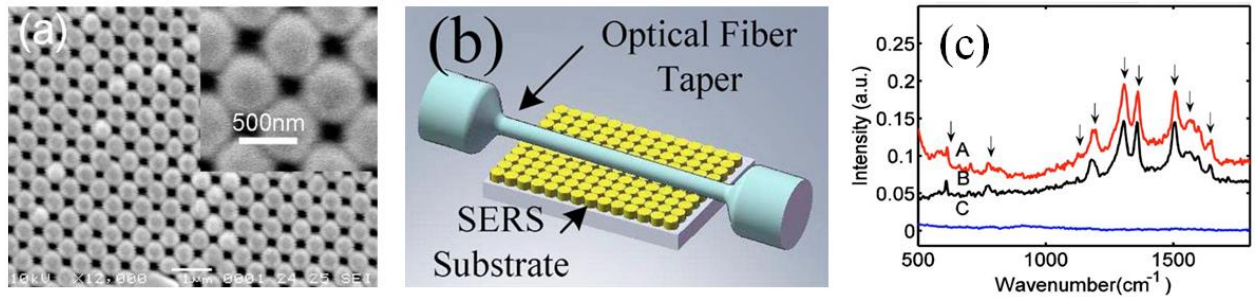


**Fig. 10.9.** (a) SEM image of an  $\text{As}_2\text{S}_3$ -based SERS substrate prior to gold coating; (b) Schematic configuration of a fiber-taper-coupled SERS substrate; (c) Raman spectra of Rhodamine-6G obtained with A, fiber-taper-coupled SERS substrate; B, conventional free-space laser-focusing method; and C, fiber-taper on a smooth gold surface. where arrows indicate Rhodamine-6G vibrational modes (Image courtesy  $\text{As}_2\text{S}_3$  glass leads to major increase of its chemical resistance to amine etchants. Subsequently wet chemical etching was used to sculpt the 3-D nanostructure (Fig. 10.9a). A thin layer of gold is sputtered on top of the chalcogenide nanostructure to form the SERS substrate. Raman enhancement of the SERS substrate was tested using Rhodamine-6G molecules. The excitation light was delivered to the substrate either via conventional microscope focusing or by evanescent excitation from a tapered multi-mode optical fiber (Fig. 10.9b). Raman signal enhancement factors up to  $2.1 \times 10^6$  was reported using the fiber evanescent excitation configuration, which is over an order of magnitude higher than SERS signals generated from Rhodamine-6G solutions containing silver colloidal nanoparticles [115]. The proof-of-concept demonstration shows that the photosensitive patterning technique offers a potentially low-cost top-down fabrication alternative for SERS substrate processing.

## 10.3 FIBER SENSORS

### 10.3.1 *Introduction*

Optical chalcogenide glass fibers have undergone tremendous development since the first draws were reported in the mid 1960s [116]. With the advent of photonic crystal fibers, they have now found numerous applications including the fields of IR light-wave propagation [117], dispersion tailoring [118], supercontinuum generation [119], medical endoscopy [120], temperature monitoring and imaging [121-123], all-optical switching [124] and Raman gain engineering [125]. In addition ChG fiber-based sensor devices have proven to be excellent candidates for remote quantitative detection and quantification of organic and biological species. Some of the key attributes of these sensors are their mechanical flexibility, length and surface area, portability, water and corrosion resistance, low environmental impact, immunity from electromagnetic fields, safety, and low fabrication cost.

The standard sensing mechanism in these applications is based on IR fiber evanescent wave spectroscopy, which consists of measuring the modulation in the evanescent electric field of the sensor fiber when in contact with an external absorbing species. Compared with oxide or fluoride glasses, IR-transmitting ChG fibers offer a much broader wavelength region available for remote spectroscopy, up to 20  $\mu\text{m}$  for the telluride-based materials. This wide spectral window in the mid-IR region overlaps the highly specific vibrational modes of most of organic chemicals and biomolecules, between 400  $\text{cm}^{-1}$  (25  $\mu\text{m}$ ) and 4000  $\text{cm}^{-1}$  (2.5  $\mu\text{m}$ ). A plethora of systems have been investigated using ChG-based fiber sensors, including aqueous and non-aqueous solutions, gaseous species, as well as solids.

Optical biosensor technology has realized remarkable developments in the last decades [126-129]. This section will specifically focus on IR fiber sensors based on chalcogenide materials. We will first describe the mechanism of evanescent wave spectroscopy, and summarize the essential properties of ChGs when used in the framework of fiber-based sensing. Finally we will present several techniques commonly employed for the shaping of ChGs into fiber optic sensors and survey their applications.

### 10.3.2 *Sensing: Infrared fiber evanescent wave spectroscopy*

When an electromagnetic wave propagates within a fiber, a part of the electric field, the evanescent wave, extends above the fiber surface. In the event of a coupling between the travelling wave and an absorbing medium, energy transfer can occur and a vibrational spectrum specific to that medium can be recorded. The sensing mechanism used by ChG fiber-based sensor technology makes use of this effect by monitoring the modulation in the evanescent wave when the fiber is put in contact with an external absorbing substance. This analytical method, commonly called Fiber Evanescent Wave Spectroscopy (FEWS), has been extensively studied [130-132]. Unlike other IR spectroscopy techniques, the measuring beam does not need to travel through the sample to extract useful information from the medium; FEWS is of particular interest for samples that scatter or are opaque in the IR wavelengths.

FEWS sensors are similar to Attenuated Total Reflection (ATR) spectrometers, however unlike standard ATR crystals, the elongated configuration of the fiber ensures a longer waveguide/medium. This in turn generates a larger number of internal reflections, thus enhancing detection sensitivity.

The experimental setup for FEWS consists of a Fourier Transform Infra Red (FTIR) spectrophotometer coupled with an IR fiber and a mercury cadmium telluride (MCT) detector (Fig. 10.10a). The signal is collected on a computer and interpreted using conventional spectral analytical tools.

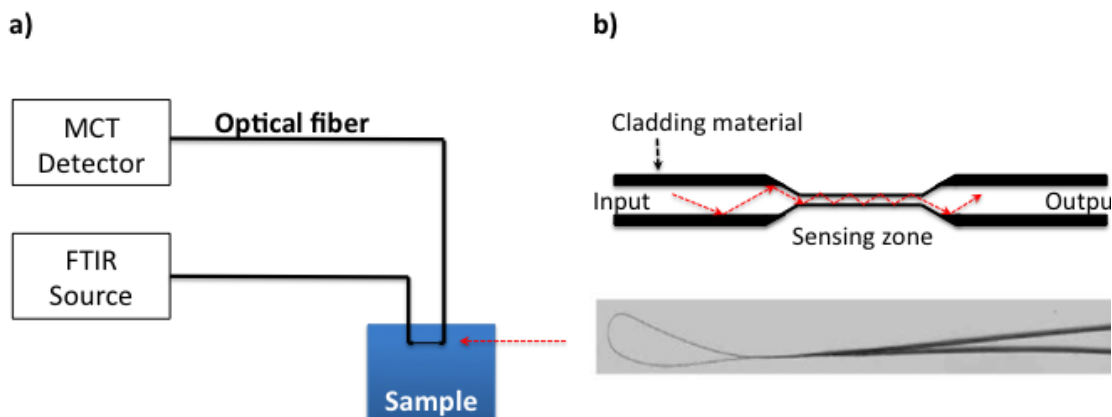


**Fig. 10.10.** A FEWS experimental set up **(a)** A tapered ChG fiber, connected to an FTIR spectrophotometer and an MCT detector, is put in contact with the sample; **(b)** Schematic

Here, the fiber is dipped into the analyte medium and interacts with the sample along a thin section, called the sensing zone (Fig. 10.10b). In fact, it has been demonstrated that the sensitivity of the measurement is inversely proportional to the diameter of the sensing fiber [134, 135]. Thus an efficient way to increase the signal-to-noise ratio is to reduce its cross-section, typically to 100  $\mu\text{m}$  or smaller. The sensing zone is generally a few centimeters long, which results in a trade-off between enhancement of the length of the interacting zone to increase absorption, and conservation of the mechanical integrity of the whole fiber. The reduction of the diameter of these fibers is achieved either by a sharp increase of the capstan speed during the fiber drawing, and/or the congruent etching of the glass fiber [135, 136]. Recently Lepine *et al.* [137] have proposed a new method based on optical micro-fabrication processing to fabricate tapers with fine control of the dimension.

### 10.3.3 Material requirements

Chalcogenide glasses are covalently bonded amorphous semiconductors, which contain either sulfur (S), selenium (Se) and/or tellurium (Te). These elements are combined in a continuous fashion with glass-formers such as As, Sb, Ge or Ga in order to tune their thermo-mechanical and optical properties. Due to their heavy constituent elements, ChGs are low-phonon energy materials. Unlike oxides glasses, which have their phonon absorption energy in the 1000  $\text{cm}^{-1}$  region (IR cut-off around 2 to 3  $\mu\text{m}$ ), sulfide-based glasses typically transmit light up to 12  $\mu\text{m}$ , selenides to 16  $\mu\text{m}$ , and tellurides to 20  $\mu\text{m}$ . As noted earlier the large spectral windows of these glasses cover the specific vibrational spectrum of most organic chemicals and biomolecules. In addition, glassy chalcogenide materials exhibit the required combination of viscosity/temperature behavior and resistance to crystallization, which allows them to be pulled down into hair-thin cylindrical filaments of arbitrary length without devitrification. Moreover, these same optimal thermo-mechanical properties are relied upon to draw sensing zones with diameters of 100  $\mu\text{m}$  or less for higher detection sensitivity and flexibility in FEWS

sensors. Finally, ChGs exhibit hydrophobic surface characteristics and excellent resistance to chemical corrosion, which are of crucial importance for chemical and biochemical sensing.

Sulfur- and selenium-based glasses, which possess ring-like and long-chain polymeric configurations, are especially suited for forming stable amorphous phases with high transparency in the mid-IR region. Among optical fiber materials, As–S and As–Se glasses have been studied most extensively [116]. As<sub>2</sub>S<sub>3</sub> glass fibers exhibit optical losses of 12 dB/km at 3.0 μm [138] and a tensile strength of about 180 MPa [139]. Dianov *et al.* have produced As<sub>2</sub>Se<sub>3</sub> fibers with optical losses of 74 dB/km at 4.7 μm [140]. The microhardness of the As<sub>x</sub>Se<sub>100-x</sub> fibers ranges from 0.66 GPa (x = 5 % at.) to 1.04 GPa (x = 50 % at.), with a peak at 1.53 GPa for the As<sub>2</sub>Se<sub>3</sub> glass [141]. The tensile strength of unclad As<sub>2</sub>Se<sub>3</sub> glass fibers ranges from 83 MPa to 380 MPa, depending on drawing parameters [142].

The manufacturing of chalcogenide optical fibers with low optical loss is required for sensing applications. Extrinsic impurities, dissolved compounds and heterogeneous inclusions are the origin of scattering, inhomogeneity, and specific absorption bands which can interfere with light propagation through the material in the spectral region of use and/or thermo-mechanical stability [143]. In particular absorption peaks due to O–H (2.92 μm), S–H (4 μm), Se–H (4.6 μm) and molecular water (6.3 μm) can be deleterious in chemical sensing applications. Therefore ChG macroscopic preforms for thermal drawing are synthesized from ultra-high purity (5N) single chemical elements. The glass rods are obtained by melt-quenching technique in sealed silica ampoules under vacuum. In addition the mixture is subjected to supplementary impurity removal treatments, which consist in oxide volatilization, melting over hydride and oxide getters, and distillation.

#### 10.3.4 Design of ChG fiber optics for mid-IR sensing

In this section we will review the major techniques used for the fabrication of single-index, double-index and photonic crystal fibers. Ultimately the materials properties and targeted applications dictate the fabrication route.

##### 10.3.4.1 Single-index fibers

Optical fiber sensing of chemical and biological species relies on the measurement of fluctuations in the evanescent waves in the vicinity or at the surface of the device. Thus single-index ChG fibers allow direct contact with the analyzed medium, with no preliminary removal of the fiber cladding required. However, since the single-index fibers are generally highly multi-mode, taper design at the sensing zone needs to be carefully optimized to minimize mode cut-off loss. Single-index fibers are pulled from a core-only preform in a thermal draw tower (Fig. 10. 11). A preform, of typically 10 cm in length and 1 cm in diameter, is first cast in a quartz tube under vacuum. It is then placed in a draw tower composed of a heating area under controlled atmosphere, a diameter controller, a tension-meter, and a collecting drum with tunable rotation speed. The rod is locally heated above its glass transition temperature,  $T_g$ , to soften its lower part, which forms a drop. This drop is lowered down to the collection drum, where it is fixed. A few tens-of-meters of fibers with diameter in the range 100-400 μm can be collected following this procedure.

Shirayev *et al.* have obtained minimum optical losses of 0.04 dB/m at 6.7 μm for a core-only Te<sub>20</sub>As<sub>30</sub>Se<sub>50</sub> glass fiber [144]. Even though these losses are still too high for long-distance applications, they permit optical sensing on short and medium distances.

### 10.3.4.2 Double-index fibers

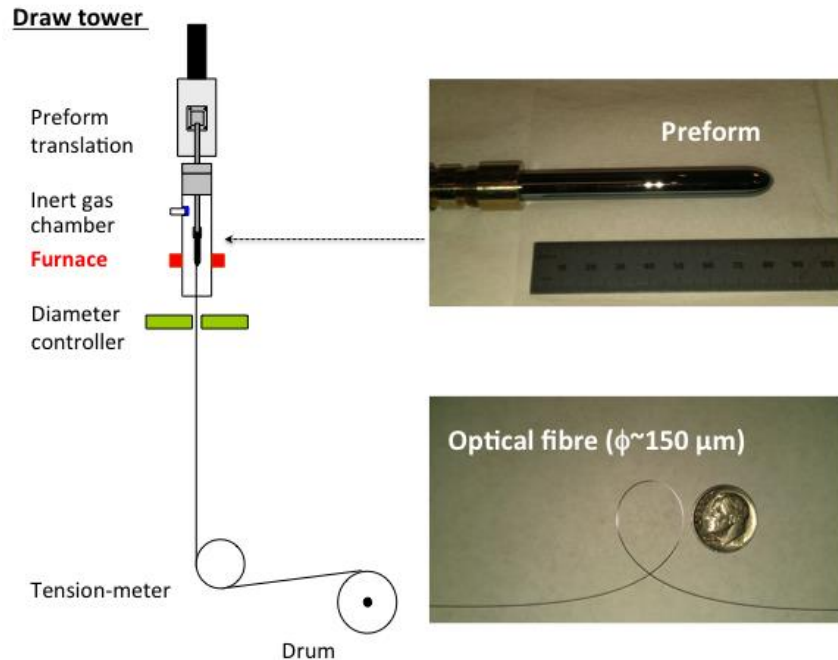


**Fig. 10.11.** Thermal drawing of a core-only preform into a single-index fiber (Pictures: Fiber optic cables guide light by Total Internal Reflection (TIR). This mechanism necessitates fibers made of two materials with slightly different refractive indices. Light travels along the core of the fiber by bouncing off the interfaces between the core and the cladding. When sensing applications necessitate long-distance or single-mode beam propagation, the fabrication of core-clad double-index fibers is required. Techniques for the preparation of solid core-clad preforms for double-index fibers are presented below.

#### Rod-in-tube technique

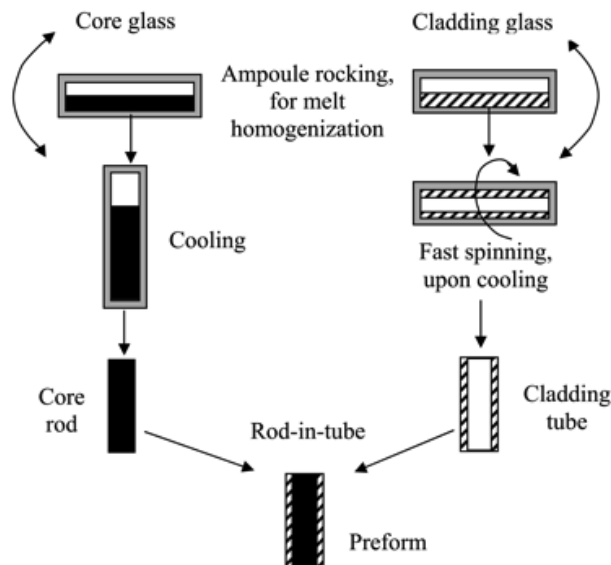


**Fig. 10.12.** Preparation of double-index preform by the rod-in-tube technique (Image

The preparation of ChG preforms by the rod-in-tube technique is a 2-step process [145, 146], as shown in Fig. 10. 12. It consists of two steps, firstly the synthesis of the core glass (rod) in the standard fashion, in a quartz tube under vacuum. In the meantime the cladding glass (tube) is fabricated by ‘rotational casting’, that is to say by subjecting the glass, which is first heated up above its melting temperature, to fast spinning while being cooled down below its glass transition temperature. The core-glass is finally inserted inside the cladding-glass tube and the resulting preform is drawn into meters-long fibers.

The rotational casting technique necessitates a precise control of the rotation speed and cooling rate. Moreover roughness or other defects at the core/clad interface result in detrimental scattering. The vacuum-pumping of the preform during the drawing has been shown to help improve adhesion between the core and clad materials, and thus further reducing the optical losses.

#### Double crucible process

The double-crucible assembly consists of two silica crucibles inserted one into the other with an open nozzle at the lower end. The inner crucible is charged with the core glass while the outer crucible contains the cladding glass. The system is raised to temperature under an inert atmosphere in the vicinity of the nozzle to soften the glasses. The core/clad glasses are then co-drawn into a fiber through the nozzles. The double-crucible assembly was successfully used for the drawing of core/clad fibers in the systems As-S, Ge-S and Ge-As-Se [148, 149]. Minimum losses were of 35 dB/km at 2.44  $\mu\text{m}$  for  $\text{As}_{40}\text{S}_{60}$ , and 148 dB/km at 1.68  $\mu\text{m}$  for  $\text{Ge}_{20}\text{S}_{80}$ , 182 dB/km at 2.12  $\mu\text{m}$  for  $\text{As}_{38}\text{Ge}_5\text{Se}_{57}$ , with diameters in the range 100-300  $\mu\text{m}$ .

#### In-situ core-cladding casting

Le Coq *et al.* developed an original technique based on the built-in casting method to fabricate double index chalcogenide fibers [150, 151]. After preparing each glass separately, the core and clad materials are introduced in a silica set-up schematically shown in Fig. 10. 13. The fabrication of the preform is achieved by a series of two separate vacuum distillations, followed by the in-situ casting of the preform through sequential rotation of the system. The demonstration of the potential of this technique for the fabrication of double-index preforms has been realized with the glasses  $\text{Te}_{25}\text{As}_{30}\text{Se}_{45}$  (core) and  $\text{Te}_{20}\text{As}_{30}\text{Se}_{50}$  (clad).

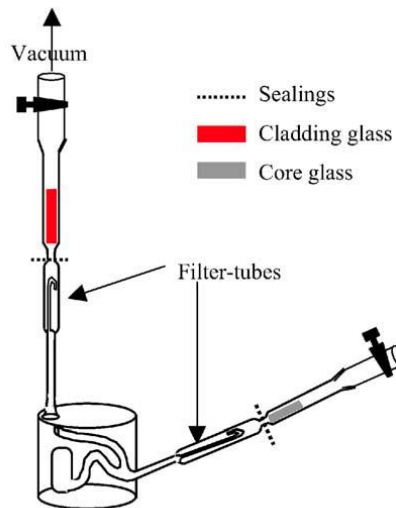


**Fig. 10.13.** Preparation of ChG preforms by in-situ core-cladding casting (Image courtesy

## Extrusion

Extrusion also allows the fabrication of core/clad preforms. Savage *et al.* successfully reported on the co-extrusion of a Ge-As-Se preform and its subsequent fiber drawing [152]. The co-extrusion technique produces preforms with optimum core/clad interface quality. Fibers with optical losses of 1.7 dB/m at 6.0  $\mu\text{m}$  were fabricated. Recently Abouraddy *et al.* have extended the technology by co-extruding composite macroscopic preforms made of two chalcogenide materials, and a thermoplastic polymer cladding [153] yielding mechanically robust fibers.

### 10.3.4.3 Photonic crystal fibers

Photonic crystal fibers have emerged as a very promising research area in recent years, with a potential for novel optical and sensing properties [154, 155]. Microstructured fibers are usually fabricated by the stack-and-draw technique. Glassy capillaries are stacked and inserted into a jacketing tube to form a preform, which is then drawn. This step can be repeated to obtain target dimensions in the final fiber geometry. Alternatively, El-Amraoui and coworkers have recently prepared preforms with a variety of geometrical patterns by direct mechanical drilling of holes in the ChG rod [156].

### 10.3.5 Applications: Optical Fibers for chemical and biochemical remote sensing

The transmission window of ChGs overlaps the 400-4000  $\text{cm}^{-1}$  IR range, which corresponds to the region of vibrational modes of organic species. This makes ChG-based FEWS an excellent tool for remote detection and analysis of a wide variety of chemicals and biochemical compounds. In this section we will review the advances and main applications of the FEWS technology, ranging from the detection of simple molecules to complex proteins and enzymes.

#### 10.3.5.1 Chemical analysis

Compton *et al.* first reported in 1988 the chemical analysis of butanone by measuring the changes in the absorbance of the fundamental vibrational peaks of the analyte along a commercially available ChG fiber [157]. Following this result Heo and coworkers used a 15 cm long GeTeSe fiber sensor to monitor the concentration of acetone, ethyl alcohol, and sulfuric acid in a solution, as well as dichlorodifluoromethane gas [158]. Since then the potential of IR-transmitting ChG-based FEWS has been expanded to the identification of a vast range of organic species, such as methanol, ethanol, isopropanol, acetone, ethanoic acid, hexane, chlorinated hydrocarbons, toluene, benzene [132, 159]. The detection limit for these substances when dissolved in water is below 3 vol. %.

Quantitative measurement of solutes samples is possible thanks to the Beer–Lambert linear relation (Eq. 10. 9), which links the absorbance and concentration as follows:

$$A(l) = \epsilon(l)LC \quad (10.9)$$

with  $A$  the absorbance,  $L$  the contact length between the probe and the solution,  $\epsilon$  the molar absorption coefficient of the surrounding media and  $C$  the concentration of the absorbent species contained in the surrounding media. As an illustration we depict (Fig. 10. 14) the analysis of ethanol aqueous solutions as a function of ethanol content [150]. This study was made with a 1.15 m long As-Se-Te core/clad fiber (core:  $\text{Te}_{25}\text{As}_{30}\text{Se}_{45}$ , cladding:  $\text{Te}_{20}\text{As}_{30}\text{Se}_{50}$ ), with a sensing zone of 90  $\mu\text{m}$  in diameter. The two absorption peaks at 9.2  $\mu\text{m}$  (C–C stretching mode) and at 9.5  $\mu\text{m}$  (C–OH vibration mode) increase with the concentration of ethanol (Fig. 10. 14a). The experiment highlights (Fig. 10. 14b) the linear relationship of the absorption peak heights with respect to the concentration of ethanol.

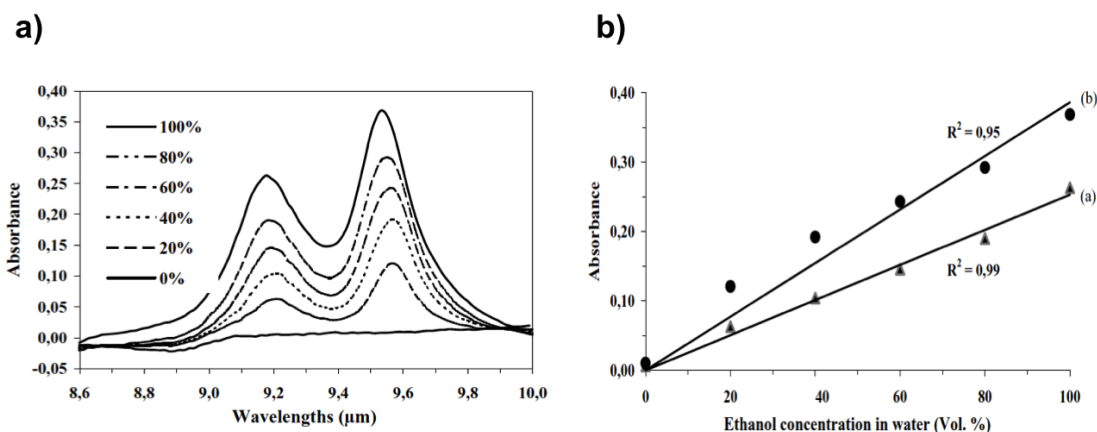


**Fig. 10.14. (a)** Absorbance of ethanol in water for different concentration; **(b)** Absorbance (peak heights) vs. ethanol concentration for the bands at (a) 9.2 μm and (b) 9.5 μm (Image courtesy of

Remote IR fiber-based spectroscopy allows real-time exploration of chemical reactions, and as a consequence, provides a valuable tool to access information on complex reaction mechanisms. For instance Anne *et al.* [160] have monitored in real-time, the polymerization process of an industrial thermo-hardening resin using a Ge-Ga-Sb-Se optical fiber, while Li *et al.* employed a similar process to characterize the polymerization of styrene films [161]. In the food industry, Le Coq *et al.* quantitatively monitored the conversion of fructose and glucose into ethanol during the fermentation process of cider [162]. Differentiation of egg's white versus yolk has also been demonstrated [163].

FEWS offers a convenient and flexible tool for the detection of gaseous species. Taga *et al.* [164] have detected several single gaseous species - such as hexane, trichloro-trifluoro-ethane, methane, acetone, etc. - as well as gaseous mixtures in concentration ranges of 1–10 vol.% with a ChG fiber optic coupled to an FTIR spectrophotometer. In the environmental field, work is in progress to demonstrate the potential of ChG fibers for the control of greenhouse gas emissions, notably carbon dioxide. Using a specifically tuned micro-structured Ge<sub>20</sub>Se<sub>40</sub> fiber, the detection of CO<sub>2</sub> has been measured to the limit of 20 vol.% [165]. In the medical field, Yoo *et al.* [166] have developed a fiber optic respiration sensor capable of detecting carbon dioxide in the exhalation of a patient. Unlike conventional electrical sensors or transducers, these fibers can be inserted in high electro-magnetic field environments such as magnetic resonance imaging devices, with no risk of signal interference. This result is expected to be highly suitable for real-time monitoring of respiratory activity in clinical situations.

### 10.3.5.2 Pollution monitoring

Mid-IR sensor systems can be used on-site for the determination of organic pollutants in soils, aquifers, and marine environments. For instance Sanghera *et al.* deployed (Fig. 10. 15) a 20-m-long fiber combined with a portable FTIR unit and a cone penetrometer to detect diesel fuel contamination in soils and marine sands [167].

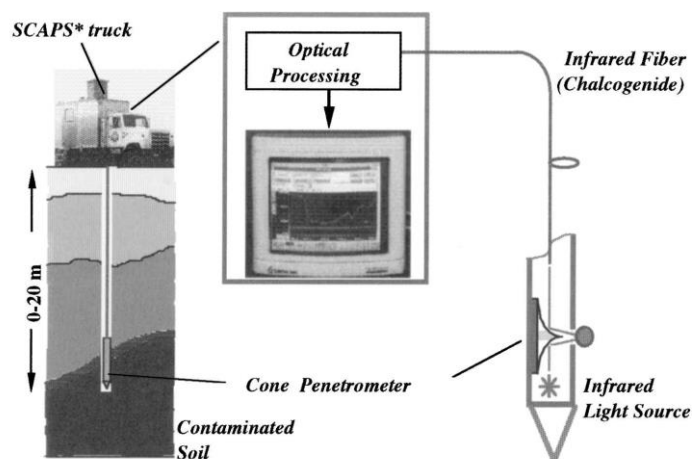


**Fig. 10.15.** Cone penetrometer system using ChG fiber for detection of contaminants in

Furthermore, preliminary pilot scale tests were led in an artificial aquifer with a 2 m long flexible  $\text{As}_{20}\text{Se}_{30}\text{Te}_{50}$  fiber [168]. The study showed that FEWS enables detection of weak concentrations of pollutants, down to 1 ppm for chlorinated hydrocarbons, specifically  $\text{C}_2\text{Cl}_4$ , in the aquifer inlet as a function of time. These studies illustrate the potential of ChG-based FEWS-integrated devices, which could be permanently installed on site for real-time pollution monitoring.

### 10.3.5.3 Biochemical analysis

The mid-IR region encompasses the spectroscopic fingerprint regions of biological molecules, microorganisms, and tissue. The probing of this region enables researchers to detect biochemical alterations related to critical phases in development biology, and to resolve these changes both spatially and temporally.

In-vivo fiber-based spectroscopic analysis on tissues has been shown to offer a valuable tool to orient and facilitate medical diagnostics [169, 170]. Hocde *et al.* used FEWS to identify metabolic alterations in laboratory animals [136]. For this the authors compared the spectral trace of biological fluid serums extracted from the blood samples of healthy and obese mice. FEWS has been successfully used to control in real-time the glucose level of human patients after they received intravenous glucose injections [171]. Non-invasive measurements were performed through the mucous membrane of the lips of a patient, a promising result for diabetes control. Similar FEWS in-vivo measurements have been carried out on anesthetized live animals for premature tumor detection [167].

FEWS allows the monitoring of metabolic processes remotely in live cells by guiding the fiber sensor onto the area of interest. Thus live microorganisms, cell cultures, and tissue explants can be probed directly within a specifically designed experimental setup without the need for biopsy. As an example, Keirsse *et al.* have mapped in real-time with an As-Se-Te fiber sensor the dynamics of population for a *Proteus Mirabilis* cell colony during the swarming of biofilms [172, 173]. The experimental setup is depicted in Fig. 10. 16. The tapered sensing zone of the fiber is put into contact with the gelose beyond the periphery of the biofilm. The alternation of bright versus black rings on the micrograph highlights the periodicity of the swarming process and the radial direction of mass migration.

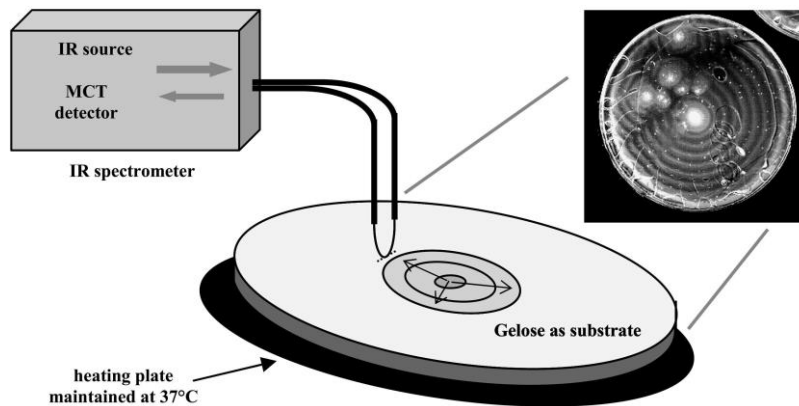


**Fig. 10.16.** Scheme of the experimental set-up used for the monitoring of biofilm (Image courtesy of [173])

Furthermore FEWS-based live cell monitoring offers an efficient technique to evaluate metabolic responses of human lung cells exposed to various toxicants [174]. These results demonstrate the potential of ChG-based FEWS for the design of bio-optic sensors able to respond in minutes to the presence of toxic agents.

### 10.3.6 Other ChG-based fiber sensors

The term ChG-based fiber optic sensor covers a broad range of devices that work in many different ways. Besides chemical and bio-chemical species sensing, this technology has proven very efficient in the probing of physical parameters such as temperature, pressure, and mechanical deformation.

#### Single-mode infrared fibers for space sensing

Under the leadership of the NASA in the US and ESA in Europe, tremendous effort is being focused in the exploration of the universe. As an illustration, the ESA's Darwin project consists of analyzing the atmosphere of extra solar earth-like planets in the 6–20  $\mu\text{m}$  spectral range in search of life; the key spectral signatures of life being represented by  $\text{H}_2\text{O}$  molecules ( $\sim 6 \mu\text{m}$ ),  $\text{O}_3$  molecules ( $\sim 9 \mu\text{m}$ ) and  $\text{CO}_2$  molecules ( $\sim 16 \mu\text{m}$ ). Thanks to their wide optical transmission spectrum and their drawing ability, the potential of low-phonon ChGs for the realization of the required wave-front filter has been extensively studied.  $\text{As}_{30}\text{Se}_{50}\text{Te}_{20}$  glass has been selected as a candidate for covering the low wavelength portion (4–12  $\mu\text{m}$ ) of the spectrum of interest [175]; to cover the 12–20  $\mu\text{m}$  region, new glass compositions are under consideration. A single-mode  $\text{As}_{30}\text{Se}_{50}\text{Te}_{20}$  fiber with an attenuation of 0.1 dB/m at 10.6  $\mu\text{m}$  has been fabricated. Systems based solely on tellurium as the chalcogen (i.e. glasses in the Ga-Ge-Te system), exhibit transparency windows extending up to 25  $\mu\text{m}$  [176–178]. A drawback, however, results from the addition of tellurium as it drastically decreases the glass network's resistance towards crystallization. This attribute makes the shaping of these promising materials, challenging.

#### Microbending sensors

Intensity-modulated fiber sensors measure the variation in the intensity of light traveling through the device as it interacts with an external physical perturbation. Miclos *et al.* [179] have fabricated ChG fiber sensors, which rely on this principle to detect microbending applied to the device. These sensors are based on clad mode detection, with the end segment of the fiber being bent and placed in an

integrating sphere. They have a relatively simple construction, show superior sensitivity to quartz fiber optic sensors and are compatible with multimode fiber technology.

Multi-material fibers for photo-, thermal- and acoustic-sensing

Recently a new preform-based fiber processing technique has emerged that allows the simultaneous drawing of ChGs in combination with metallic electrodes and polymers [180]. The incorporation of materials with vastly disparate optical and electrical properties into tens-of-meters-long fibers, expands the traditional functionalities of the these materials to include medical treatment [120], acoustic [181], opto-electronic [182] or electronic applications [183, 184].

As an illustration a photo-detecting device is depicted in Fig. 10. 17 [180]. The fiber is made of a thin-film  $As_2Se_3$  semiconductor in contact with four Sn electrodes, surrounded by a polyethylsulfone (PES) polymer cladding (Fig. 10. 17a). The metal electrodes are connected to an external circuit (Fig. 10. 17b). When light impinges externally on the glass, free charge carriers are generated, which yields an increase in electrical conductivity (Fig. 10. 17c). Moreover these fiber devices show (Fig. 10. 17d) dependence of their electrical resistance with temperature. Prototypes of 2D- and 3D-arrays made of multiple photo-detecting fiber have been constructed with sophisticated optical and imaging functionalities [182].

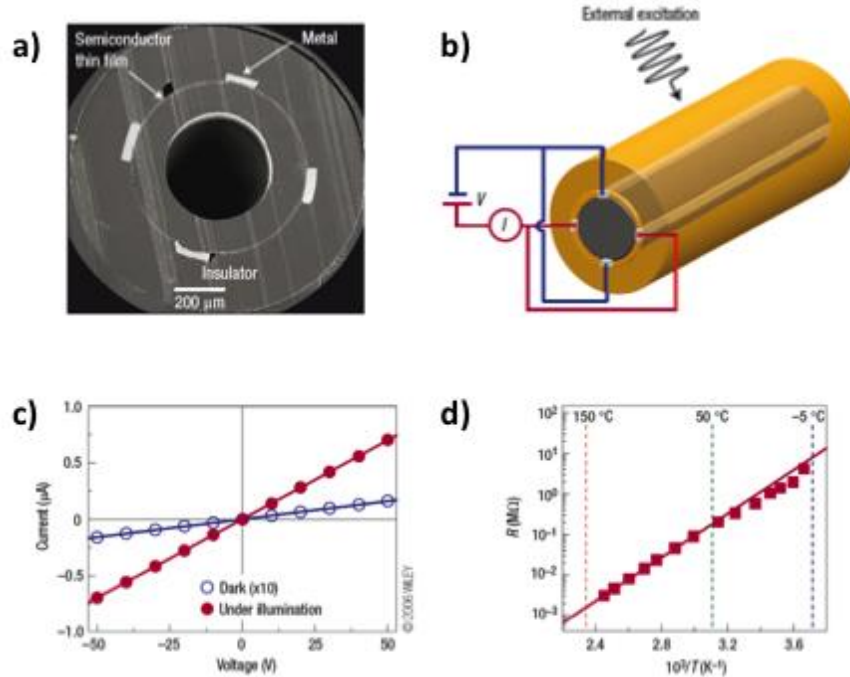


**Fig. 10.17.** Photo-detecting fiber device **(a)** SEM micrograph of a thin-film fibre device (semiconductor:  $As_2Se_3$ , polymer: PES, metal: Sn); **(b)** Electrical connection of the metal electrodes at the periphery of the fibre; **(c)** I-V characteristic curve of a 15-cm-long photo-

## 10.4 CHG COMPOSITIONAL DESIGN FOR SENSING

### 10.4.1 *Material Properties for Sensor Design*

Previous sections have demonstrated the use of ChGs in a wide variety of fiber and thin film sensing devices, which requires specific knowledge of the optical, thermal, and mechanical properties of the ChG in use. In general, these material characteristics largely fall into two main categories: optical, and thermal (as well as some application-specific factors such as chemical resistance or radiation hardness).

Optical characteristics of interest to materials engineers include the glass' optical transparency window, the refractive index of the glass, and index dispersion or  $dn/dT$  effects if the application demands broadband optical or wide-ranging thermal use. Thermal characteristics of interest include the crystallization window (which is defined by the temperature range between the glass' transition temperature and any onset of crystallization), the coefficient of thermal expansion (CTE) of the matrix, and the viscosity-temperature dependence of the composition and thermal conductivity (which is an important material parameter for thermal management in on-chip photonic circuits). The following sections describe these material design factors in the context of their composition dependence, with an eye towards the next section, which will discuss the problem of correlation between material design properties.

#### 10.4.1.1 *Transparency Window*

The transparency window, or spectral region over which the ChGs does not absorb optical energy, is critical in designing any of the sensor systems discussed previously. ChGs retain their optical transparency over a wide range of the IR region of the spectrum, extending as far as 20  $\mu\text{m}$ . This remarkable transparency window is shown in Fig. 10. 18 in comparison to some other glass types.

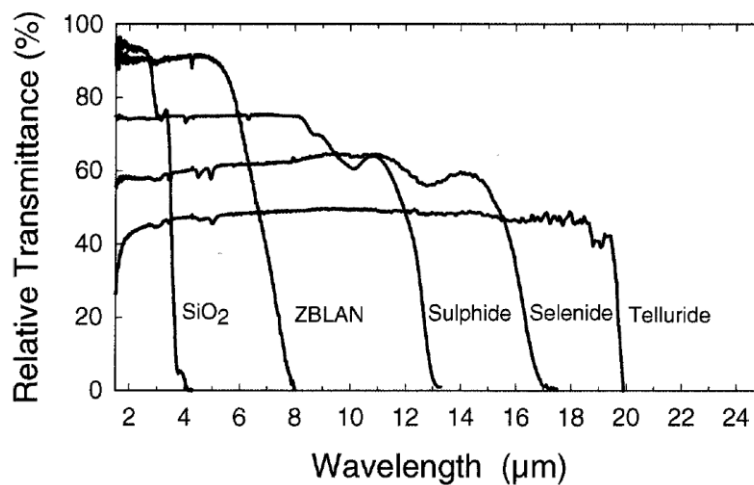


**Fig. 10.18.** Transparency windows for several glass types. Some telluride glasses are transparent past 20  $\mu\text{m}$  (Image courtesy of [167]).

As noted in previous sections, IR transparency is critical in biological and chemical sensing applications because most organic chemicals have characteristic absorptions in the spectral region between 2.5 and 20  $\mu\text{m}$ , making IR spectroscopy a valuable tool in detecting toxins [185], sensing temperature in extreme environments [121], and searching for life in the universe [177]. Optimizing transparency for sensing applications often involves purification of the ChG to remove any impurities, which may cause scattering or have absorptions of their own in the IR region, thus limiting detectivity of target analytes. In the context of the transparency window it is important to note that the absorption peaks due to O-H (2.92  $\mu\text{m}$ ), S-H (4  $\mu\text{m}$ ), Se-H (4.6  $\mu\text{m}$ ) and molecular water (6.3  $\mu\text{m}$ ) are prime targets for purification, as these intrinsic absorbances can interfere with the sensing application, especially in planar and fiber schemes where the optical path length is sometimes very long [186].

#### 10.4.1.2 *Refractive Index*

ChGs are known for their relatively high index of refraction. As an illustration the refractive index at  $\lambda = 3 \mu\text{m}$  is  $n = 1.44$  for  $\text{SiO}_2$ , whereas  $n = 2.80$  for  $\text{As}_{40}\text{Se}_{60}$ , which is a prototypical chalcogenide composition. This illustrates the magnitude of the difference between the refractive indexes of oxides and those of the ChGs. One of the results of this high refractive index is the commensurately high Fresnel Reflection loss, as shown in the baseline relative transmittance of the ChGs in Fig. 10. 18 above, which indicates that between 25 and 50% (depending on composition) of the incident light is lost in single surface (times 2) reflection loss. A number of advantages can be gained from the high refractive index of ChGs, however. Their comparatively high index makes them prime candidates for high index contrast structures useful in wave-guiding and planar sensing devices [23, 71] where high contrast translates to small feature sizes, maximizing the optical function to real estate trade-off. The high linear refractive index also implies a high nonlinear refractive index, and ChGs are proving useful as nonlinear optical materials in a number of systems [187].

Precise knowledge of the refractive index of the materials in the system is needed for optical design models to correctly predict things like the shapes of lenses. However, the refractive index of the ChG may be impacted by the processing conditions experienced during fabrication of the sensing structure (thermal evaporation of films, fiber tapering) and by any post-processing heat treatment. Because these processing conditions require heating the glass to near or past its glass transition temperature, atomic-level structural rearrangement can occur in the glass network which would be reflected as a change in refractive index. Fig. 10. 19 below shows the impact of thin film deposition route, either Pulsed Laser Deposition (PLD) or Thermal Evaporation (TE), and post-deposition thermal annealing on the refractive index of  $\text{Ge}_{23}\text{Sb}_7\text{S}_{70}$  films. Because of the ultra-short timescale of the film deposition during PLD, the glass network is “frozen in” much further away from thermal equilibrium than in the melt-quenched and annealed bulk piece, for which the refractive index is also shown in the figure. This difference in network structure induced by the processing route is reflected by the large gap ( $\sim 0.1$ ) in refractive index between the as-deposited PLD film and the parent bulk glass.

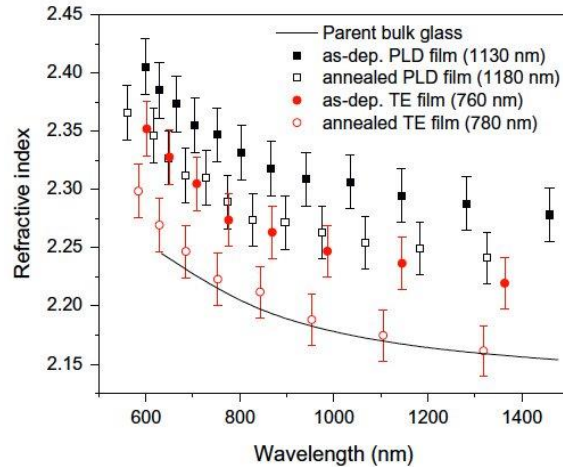


**Fig. 10.19.** Refractive index dispersion for TE and PLD films as estimated from fitting of the transmission spectra. The solid line represents the dispersion of the bulk glass from which the films were deposited (Image courtesy of [188]).

In both the TE and PLD films, post-deposition annealing was successful in at least partially returning the index of the film to that of the bulk glass. In the case of the PLD films, due to the rapid-quenched structure discussed above, even a thermal anneal cannot fully relax the structure back to that of the original bulk glass, and the refractive index in these films remains higher across the IR spectral range than those of the parent glass.

#### 10.4.1.3 Dispersion and the Thermo-Optic Coefficient

Depending on the application of the particular chemical or biological sensing device, the change in refractive index with wavelength ( $dn/d\lambda$  or dispersion) or temperature ( $dn/dT$  or thermo-optic coefficient) may be important, especially in the long-pathlength structures sometimes found in both planar [70] and fiber [133] geometries. Fig. 10. 20 shows the refractive index dispersion of  $Ge_{23}Sb_7S_{70}$  films over the 0.6 to 10.6  $\mu\text{m}$  wavelength range; as can be seen, the refractive index varies by 0.155 over the near- to mid-IR spectral range, which is large enough that it must be clearly accounted for in applications of this material which demand a large optical bandwidth [15]. Mid-IR sensing applications benefit from a relatively flat index change between 2 and 6  $\mu\text{m}$ , the changes in slope evident at the short and long wavelength ends of the spectrum are due to the onset of absorption due to bandgap excitations at short wavelengths and multi-phonon absorptions at longer wavelengths. The shape of the dispersion curve is characteristic of almost all optical glasses, and has been fit in Fig. 10. 20 using the Sellmeier Equation to extract parameters, which can be compared to other materials in the same glass family.

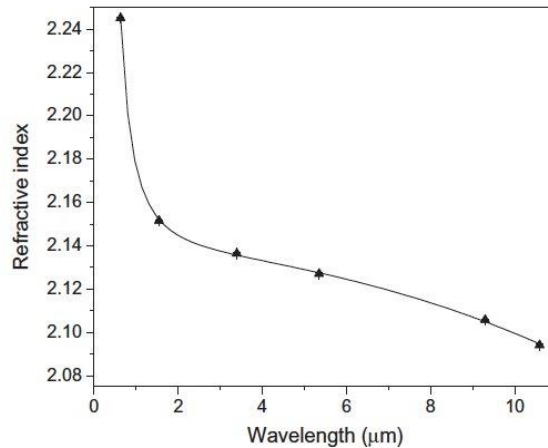


**Fig. 10.20.** The refractive index dispersion of  $\text{Ge}_{23}\text{Sb}_7\text{S}_{70}$  films over the 0.6 to 10.6  $\mu\text{m}$

The thermo-optic (TO) coefficients of ChGs in particular, and optical materials in general, are much less well-characterized than their optical dispersions and Sellmeier parameters. Additionally, data on the compositional variation in TO for ChGs is minimal as compared to the extensive compendium of such data for commonly employed oxide glass materials. Many times in current optical designs, the change of refractive index with temperature is estimated on a best-guess basis using known values from a reference material. Depending on the glass composition, the TO coefficients of ChGs span a wide range from a few tenths to over 100 ppm/K<sup>-1</sup> [189]. Though not themselves ChGs, the IR-transparent crystals of silicon and germanium have been extensively studied, and will have to substitute for discussion of the actual ChGs, for which very little data exists [190]. Fig. 10. 21 shows the change in refractive index of silicon and germanium crystals as a function of temperature. The data in this figure has been extracted from the excellent work on the subject being conducted by NASA [191]. Note the break in the Refractive Index axis used to accommodate both materials in the same figure.

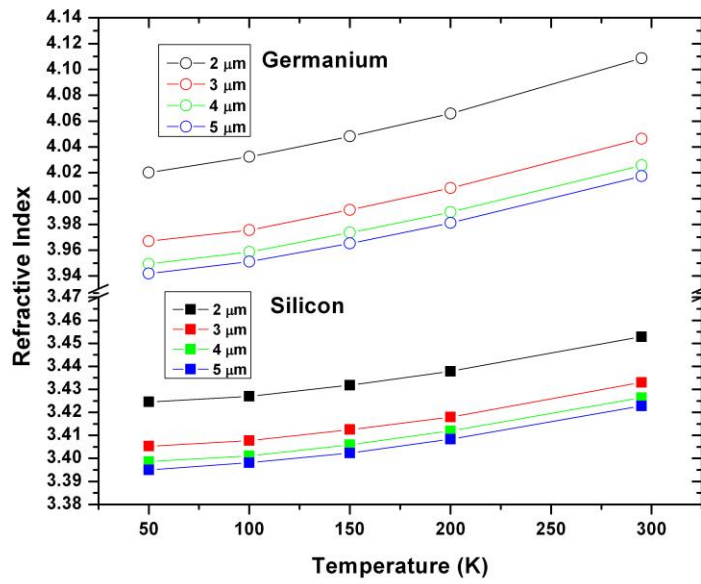


**Fig. 10.21** The change in refractive index of silicon and germanium crystals as a function

In this case the change in refractive index with a change in temperature is positive, rather than the negative change in the case of wavelength shown in Fig. 10. 20. As a reference, the change in refractive index dispersion for these materials measured by NASA is shown in Fig. 10. 22 below.

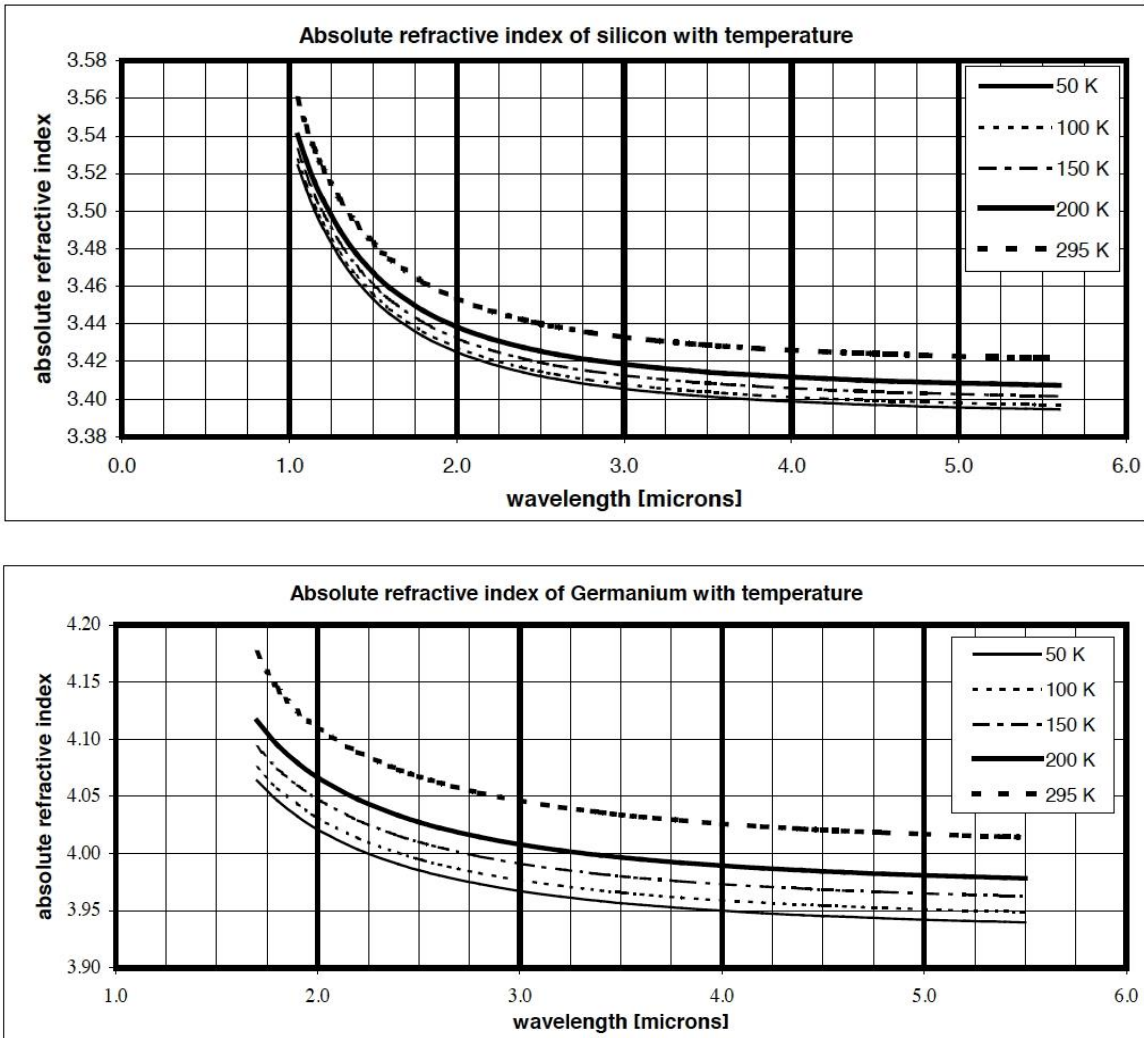


**Fig. 10.22.** Optical dispersions of silicon and germanium as a function of temperature (Image

As noted above, Fig. 10. 21 and Fig. 10. 22 show the same data, but plotted on different scales. An accurate optical design for a sensing application, which requires high optical bandwidth as well as well-characterized temperature response, ie. sensors that will be deployed in harsh environments to detect a range of chemical and biological signatures, would ideally characterize these two impacts on the refractive index (thermal and optical) as part of a larger suite of materials parameters. Additionally, these data will be critical in the design of resonant cavity structures, fabricated for example on Si chips, in determining the thermo-optic wavelength drift. On the other hand, the high TO coefficients in selected ChG compositions may be exploited for highly sensitive photothermal detection. The idea of cross-correlations between these thermal and optical parameters will be discussed in greater detail in Section 10.4.2.

#### 10.4.1.4 Crystallization Stability

A good guide for the usability of a particular ChG composition for planar and fiber sensing applications is knowledge of the glass' crystallization window  $\Delta T$ , where  $\Delta T = T_x - T_g$ . This metric defined as the temperature difference between the onset of crystallization (if present) and the material's glass transition temperature, gives the temperature range over which the material can be shaped without crystallizing. The actual temperature needed to shape the ChG into the fiber or thin-film form may be anywhere (and even in some cases outside!) of this range, but  $\Delta T$  is a good metric for the relative ease of formability of various ChGs, some of which are shown in Table 10.1.

**Table 10.1.** Variation in some thermal properties of the ternary Ge-As-Se glass system (Data originally presented in [192]).

Composition	$T_g$ (°C)	$T_x$ (°C)	$\Delta T$ (°C)
Se	37	96	59
Ge <sub>25</sub> Se <sub>75</sub>	220	375	155
Ge <sub>25</sub> As <sub>10</sub> Se <sub>65</sub>	297	478	181
Ge <sub>30</sub> As <sub>30</sub> Se <sub>40</sub>	373	478	105
Ge <sub>20</sub> As <sub>40</sub> Se <sub>60</sub>	313	521	208

The crystallization window  $\Delta T$ , and near the highest crystallization temperatures, giving them much greater  $\Delta T$  values than the simpler Se and As<sub>40</sub>Se<sub>60</sub> glasses. This increase in crystallization stability makes Ge-containing ChGs very attractive for fiber applications, where stability against crystallization during fiber drawing or tapering is critical in maintaining optical transparency. However, a trade-off to this material stability is the higher cost of Ge, as compared to the other constituents shown.

#### 10.4.1.5 Coefficient of Thermal Expansion

The coefficient of thermal expansion, or CTE, is a measure of the mechanical response of a glass network to an applied thermal load. While of vital importance for bulk optics and their application in optical systems, sensing systems based on planar or fiber forms of similar or dissimilar materials require knowledge of CTE as it impacts the ability to maintain both material geometry and TO behavior. The linear expansion of a system in response to an increase in temperature is thus written as:

$$dL = \alpha_L L dT \text{ or } \alpha_L = \frac{1}{L} \frac{dL}{dT} \quad (10.10)$$

where  $L$  is the length of the sample at room temperature,  $dL$  is the change in length,  $dT$  is the change in temperature and  $\alpha_L$  is the linear CTE. Because the CTE measurements are typically performed below the glass transition temperature, there is no contribution to the thermal expansion from conformation or bonding changes in the material; the expansion is a reflection of the aggregate change in interatomic bonding distances. In general, as the temperature of a glass is increased in the region below  $T_g$ , the additional thermal energy permits the elongation of the mean bond length as dictated by the shape of the potential energy well representing the bond [193].

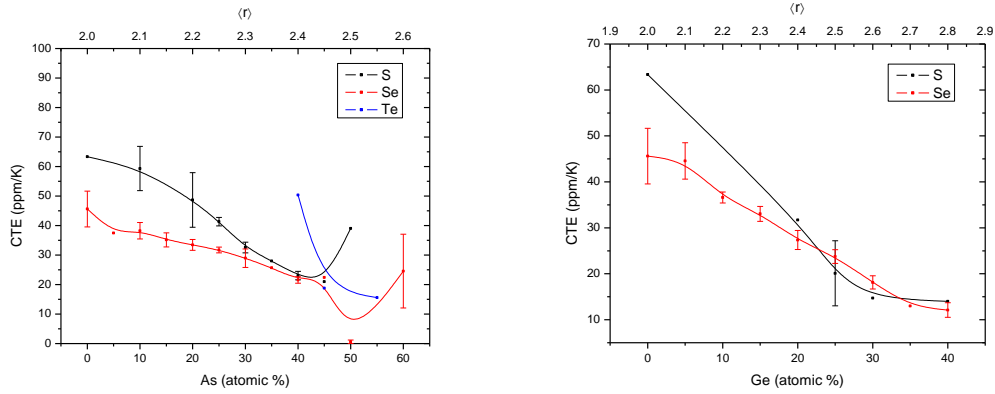


**Fig. 10.23.** Variations in CTE for arsenic- and germanium-based binary ChGs.

As shown in Fig. 10. 23, in the arsenic system, the evolution of the measured CTE with As % follows a almost linear trend win both the sulfur and the selenium based systems, with an apparent local minimum at the stoichiometric  $As_{40}S_{60}$  ( $\langle r \rangle = 2.4$ ) composition, and a similar local minimum at the slightly arsenic rich composition of  $As_{50}Se_{50}$ . Following these minima, the linear trend is no longer evident, as the CTE begins to rise with increasing arsenic content before leaving the glass forming region.

#### 10.4.1.6 Viscosity

For both planar and fiber sensing applications, a precise understanding of the variation of glass viscosity ( $\eta$ ) with temperature ( $T$ ) has been shown to be critical in the creation of high performance optical systems from ChGs. For fiber applications, definition of this  $\eta/T$  relationship is an important design parameter to enable defect-free drawing of the engineered glass into fiber of usable lengths, and to permit subsequent tapering to increase detection sensitivity in devices. ChGs in general have a much more pronounced variation of viscosity with change in temperature than do the oxide glasses. This drastic variation in viscosity in ChGs, from a barely softened solid to essentially a liquid within a 100 °C range, means that there is a much tighter temperature window over which these glasses can be

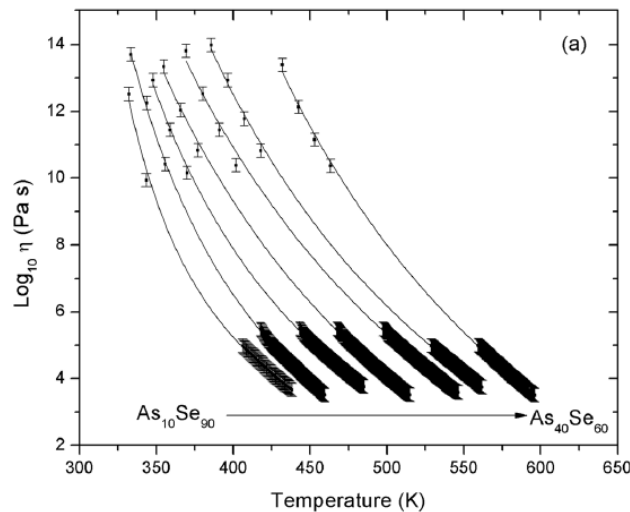


**Fig. 10.24.** Viscosity curves for the  $As_xSe_{100-x}$  glass family from  $x = 10$  (leftmost) to  $x = 40$  (rightmost) obtained through beam bending and parallel plate viscometry (Image

made into fiber than their silicate counterparts. As shown in Fig. 10. 24, the viscosity/temperature behavior of a ChG glass family varies as a function of the elemental ratios, which is an important design characteristic and can strongly impact the choice of glass matrix for a given application.

As shown in the figure, the viscosity/temperature curves for the arsenic selenic glass family shift nearly uniformly to higher temperatures as the molar fraction of arsenic is increased in steps from 10 to 40 % in the system, meaning that the higher selenium content glasses can be processed via thermal routes at very low temperatures; however, the viscosity changes very rapidly with temperatures in these selenium rich compositions, which makes some fiber fabrication routes very difficult to control accurately.

Some applications necessitate extremely detailed knowledge of the liquid viscosity of the glass in their design, as they require liquid-like flow of the glass to form or optimize the sensor structure. Fig. 10. 25 shows the use of a thermal reflow process to reduce the surface roughness of photolithographically-patterned waveguides of ChGs [194]. Reduction of the sidewall roughness in these waveguide structures leads to dramatic reduction in their scatter loss, which is very important as they serve as the transmission lines in a chip-scale IR sensing device.

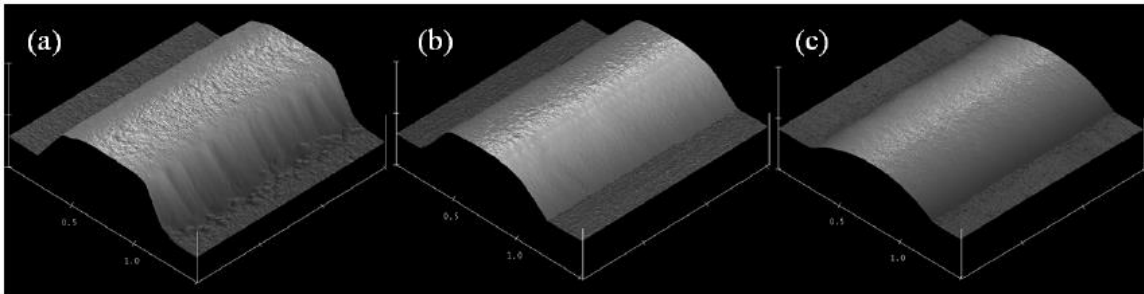


**Fig. 10.25.** Surface morphology of  $\text{As}_2\text{S}_3$  chalcogenide waveguides measured by AFM (a) as-patterned; (b) reflowed at 230 °C for 15 s exhibiting reduced sidewall roughness; and (c) reflowed at 245 °C for 15 s showing significant cross-sectional geometry modification (Image courtesy of

#### 10.4.2 OPTIMIZATION OF MATERIAL DESIGN THROUGH CORRELATION STATISTICS

To introduce the ideas used in optimization of material design, let us return to the problem of the dispersion and thermo-optic coefficient as introduced in Section IV.2. In short, the refractive index of the sensing medium (ie. the chalcogenide glass) can vary as a function of the wavelength of the incident IR light, known as dispersion or  $dn/d\lambda$ , but also as a function of the temperature, characterized by the TO coefficient,  $dn/dT$ . Let consider a sensor design, which requires operation over a large range of the IR spectrum (from 1 to 20  $\mu\text{m}$ ), and will be deployed in a hostile environment in terms of exposures to broad temperature ranges. For this type of sensor to operate robustly, both the dispersion and thermo-optic coefficient of the ChG need to be accurately characterized and optimized. The combined impact of wavelength and temperature on the refractive index of germanium, Ge, and silicon, Si, crystals at cryogenic temperatures is shown in Fig. 10. 26.

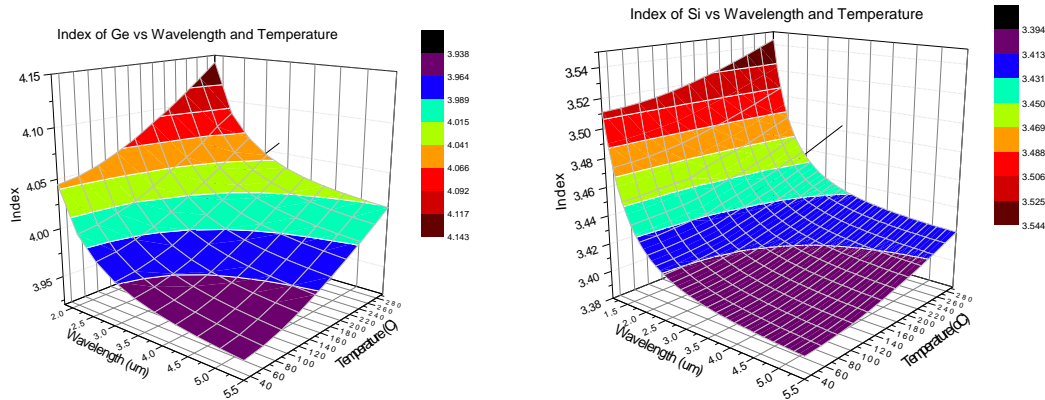


**Fig. 10.26.** Variation of refractive index as a function of wavelength and temperature for crystalline germanium and silicon. Data from [191] used to generate figures, which themselves are courtesy of

Ideally, the job of the optical materials engineer is to use compositional design to conform exactly to sensor design specifications. In reality, the situation often reduces to making a series of prioritizations of design characteristics and a thorough understanding of the tolerances, then making materials decisions based on compositions which best fit these sensor design criteria. The question then becomes one of identifying the optimal composition to meet these specifications, and how to arrive at the best solution without resorting to trial and error or settling for tried-and-true solutions in the interests of speed.

A rapid, first-order solution can be obtained through the use of the statistical method of correlation coefficients as a guide to the exploration of composition space. The Pearson Correlation Coefficient,  $r$ , is a measure of how linearly a measured property changes in response to a given variation in the elemental ratios during composition design. Values of  $r$  close to  $\pm 1$  indicate perfect correlation or anti-correlation, while values of  $r$  closer to 0 indicate the lack of any statistical correlation between the change in composition and the change in property.

To clarify the details of the process of using  $r$  to design glass compositions, Table 2 shows the elemental compositions, thermal, and optical properties of Schott's IG series of glasses as taken from their published datasheets.

**Table 2.** Compositions, optical, and thermal properties of Schott's IG series of Glasses [189].

Trade Name	Composition	$\lambda_{mi}$ (μm)	$\lambda_{ma}$ (μm)	$\Delta\lambda$ (μm)	n @ 10 μm	dn/dλ @ 10 μm (μm <sup>-1</sup> )	dn/dT @ 10 μm (ppm/°C)	CTE (ppm/°C)	T <sub>g</sub> (°C)
IG2	Ge <sub>33</sub> As <sub>12</sub> Se <sub>55</sub>	0.5	11	10.5	2.4967	108	60	12.1	368
IG3	Ge <sub>30</sub> As <sub>13</sub> Se <sub>32</sub> Te <sub>25</sub>	1	11	10	2.787	164	145	13.4	275
IG4	Te <sub>10</sub> As <sub>40</sub> Se <sub>50</sub>	0.75	11	10.25	2.6084	170	96	10.4	225
IG5	Ge <sub>28</sub> Se <sub>41</sub> Te <sub>31</sub>	0.75	11	10.25	2.6038	102	91	14	285
IG6	As <sub>40</sub> Se <sub>60</sub>	0.75	12.5	11.75	2.7775	161	41	20.7	185

$$r = \frac{\sum_{ij} \dot{a}(x_i - \bar{x})(y_j - \bar{y})}{\sqrt{\sum_i \dot{a}(x_i - \bar{x})^2 \sum_j \dot{a}(y_j - \bar{y})^2}} \quad (10.11)$$

with each of the  $x_i$  equal to the atomic fraction of an element in the composition (Ge, As, Se, etc.), and each of the  $y_i$  equal to the value of one of the thermal or optical characteristics listed in Table 2. Thus as  $r$  is calculated by indexing over all of the elemental fractions and resultant properties of the glass, a table showing the value of  $r$  for the data in Table 2, such as Table 3, gives a first-order indication of the statistical correlation between the individual elements in a glass family and the resultant thermal and optical properties.

**Table 3.** First-order indication of the statistical correlation between the individual elements in the Schott's IG series and the resultant thermal and optical properties of the glasses.

	<u>Ge</u>	<u>As</u>	<u>Sb</u>	<u>Se</u>	<u>Te</u>
$\lambda_{\min}$ ( $\mu\text{m}$ )	-0.074	0.020	0.000	-0.700	0.791
$\lambda_{\max}$ ( $\mu\text{m}$ )	-0.783	0.587	-0.250	0.414	-0.250
$\Delta\lambda_{\text{D}}$ ( $\mu\text{m}$ )	-0.738	0.563	-0.242	0.579	-0.443
$n$ @10 $\mu\text{m}$	-0.435	0.320	-0.228	-0.423	0.593
$dn/d\lambda$ @ 10 $\mu\text{m}$	-0.634	0.793	-0.652	-0.485	0.353
$dn/dT$ @ 10 $\mu\text{m}$	0.658	-0.662	0.204	-0.726	0.877
CTE	-0.975	0.912	-0.289	0.281	-0.371
$T_g$	0.902	-0.742	0.141	-0.088	0.060

Table 3 is highlighted in several areas to indicate varying levels of statistical significance. Even with this small of a sample set from which to calculate the coefficients (ie, the five SCHOTT IG glasses) it is already clear that there is a link between Ge content and the CTE of the glass: as Ge content is increased, the CTE decreases, meaning that they are negatively correlated, and strongly so as shown in Table 3. At the next level of statistical significance, Table 3 shows positive correlations between Ge and  $T_g$  as well as between As and CTE. Finally, there appears to be a positive correlation between Te and  $dn/dT$ ; however, there are too few samples in this dataset to make a guarantee.

Correlation statistics has shown to be a useful tool for the compositional design and optimization of ChGs for a wide variety of optical sensing applications. Advanced sensor designs and technologies increasingly demand more of the optical materials in terms of functionality and adherence to a wide range of optical and thermal considerations.

## 10.5 CONCLUSION AND FUTURE DIRECTIONS

Here we have described recent advances in the production of ChG-based sensing devices from a variety of thin film and fiber structures. These devices take full advantage of the broad transmission of ChGs in the IR domain, combines with their outstanding visco-mechanical behaviors and chemical stability.

In the last decades integrated planar ChG sensors have experienced significant advancement. These devices use on-chip components such as waveguides and resonators to perform complex molecular detection with a high level of selectivity. Moreover they offer several key advantages in terms of power consumption, dimensionality, or manufacturability. On the other hand, ChG-based fiber optic sensing offers an efficient and non-destructive technique to remotely detect and quantify numerous organic chemicals and biochemical substances, in liquid, gaseous, or solid forms. Current applications include, but are not limited to real-time chemical reaction control in manufacturing and food production chains, in-situ permanent pollution monitoring, and as assistance to medical diagnostic technologies. Fiber sensing is particularly useful for remote characterization of reactions that take place in non-accessible or hazardous environments. In addition the flexibility of the fibers in various forms offers great portability, and low-cost.

Future development of novel materials, device structures and sensing mechanisms will continue to improve the sensitivity and specificity metrics of ChG-based sensors. For instance, exploitation of new detection mechanisms such as the nano-cavity photothermal spectroscopy is expected to bring the detection limit of on-chip IR sensors to the same par as ultra-sensitive cavity ring-down spectroscopy. Optimization of glass device processing techniques, in particular low-loss waveguide technologies, is very likely to further raise detection sensitivity. Besides streamlining the sensor devices, optimization of surface functionalization chemistries on glass sensors will be essential for specific biological detection and may also contribute to improved sensitivity in chemical sensing through enrichment effects. Finally, we believe that emerging hybrid and monolithic integration strategies combining planar glass guided wave devices, QCLs, and on-chip detectors will ultimately pave the path towards realizing an IR spectroscopic "sensor-on-a-chip" platform. Considering fiber-based sensors, the intrinsic hollow-core structure of photonic crystal fibers offers ideal sites for liquids and gaseous species sensing, and multiple surfaces available for functionalization. Furthermore SPR has yielded in recent years the development of numerous silica-based fiber sensors for accurate and reliable sensing of optoelectronics parameters. Thus the addition to ChG-based fibers of plasmonic metal nanoparticles used for SPR sensing can open the way to sensors operating with superior performances in the near-IR region.

ChGs have demonstrated their capacity as tailorable, formable materials for IR sensing designs. At this stage of development, interdisciplinary expertise in the areas of glass science, optical physics, device processing, and surface chemistry are mandated for next-generation sensor investigation. For instance composition design through the use of statistical processes, such as the correlation coefficient approach, will contribute refining critical materials parameters, with lower losses and higher detectivity operation. Thus mastering even further ChGs chemistry, and by consequence their properties, will certainly help bringing novel materials into sensors worldwide.

## 10.6 REFERENCES

1. B. Kuswandi, Nuriman, J. Huskens, and W. Verboom, "Optical sensing systems for microfluidic devices: A review," *Analytica Chimica Acta* **601**, 141-155 (2007).
2. P. V. Lambeck, "Integrated optical sensors for the chemical domain," *Measurement Science & Technology* **17**, R93-R116 (2006).
3. S.-S. Kim, C. Young, and B. Mizaikoff, "Miniaturized mid-infrared sensor technologies," *Anal. Bioanal. Chem.* **390**, 231-237 (2008).
4. R. M. Klein, "Chalcogenide Glasses as Passive Thin-Film Structures for Integrated Optics," *Journal of Electronic Materials* **3**, 79-99 (1974).
5. B. J. Eggleton, B. Luther-Davies, and K. Richardson, "Chalcogenide photonics RID A-6012-2011," *Nature Photonics* **5**, 141-148 (2011).
6. Y. Bai, S. Slivken, S. R. Darvish, and M. Razeghi, "Room temperature continuous wave operation of quantum cascade lasers with 12.5% wall plug efficiency RID C-6716-2011 RID B-7273-2009 RID B-7265-2009," *Applied Physics Letters* **93**, 021103-021103 (2008).
7. C. Gmachl, F. Capasso, D. L. Sivco, and A. Y. Cho, "Recent progress in quantum cascade lasers and applications," *Reports on Progress in Physics* **64**, 1533-1601 (2001).
8. C. McDonagh, C. S. Burke, and B. D. MacCraith, "Optical chemical sensors," *Chemical reviews* **108**, 400-422 (2008).
9. M. Kim, C. L. Canedy, W. W. Bewley, C. S. Kim, J. R. Lindle, J. Abell, I. Vurgaftman, and J. R. Meyer, "Interband cascade laser emitting at  $\lambda=3.75 \mu\text{m}$  in continuous wave above room temperature RID A-9426-2009," *Applied Physics Letters* **92**, 191110-191110 (2008).
10. I. Vurgaftman, W. W. Bewley, C. L. Canedy, C. S. Kim, M. Kim, C. D. Merritt, J. Abell, J. R. Lindle, and J. R. Meyer, "Rebalancing of internally generated carriers for mid-infrared interband cascade lasers with very low power consumption," *Nature Communications* **2**, 585-585 (2011).
11. A. Rogalski, "Infrared detectors: status and trends," *Progress in Quantum Electronics* **27**, 59-210 (2003).
12. J. S. Sanghera, L. B. Shaw, and I. D. Aggarwal, "Chalcogenide Glass-Fiber-Based Mid-IR Sources and Applications," *Ieee Journal of Selected Topics in Quantum Electronics* **15**, 114-119 (2009).
13. Y. G. Mourzina, J. Schubert, W. Zander, A. Legin, Y. G. Vlasov, H. Luth, and M. J. Schoning, "Development of multisensor systems based on chalcogenide thin film chemical sensors for the simultaneous multicomponent analysis of metal ions in complex solutions," *Electrochimica Acta* **47**, 251-258 (2001).
14. A. E. Owen, "Chalcogenide Glasses as Ion-Selective Materials for Solid-State Electrochemical Sensors," *Journal of Non-Crystalline Solids* **35-6**, 999-1004 (1980).
15. Y. Vlasov, A. Legin, and A. Rudnitskaya, "Electronic tongues and their analytical application," *Anal. Bioanal. Chem.* **373**, 136-146 (2002).
16. V. M. N. Passaro, F. Dell'Olio, B. Casamassima, and F. De Leonardis, "Guided-wave optical biosensors RID A-5569-2010," *Sensors* **7**, 508-536 (2007).
17. A. Kovalskiy, J. Cech, M. Vlcek, C. M. Waits, M. Dubey, W. R. Heffner, and H. Jain, "Chalcogenide glass e-beam and photoresists for ultrathin grayscale patterning RID

- A-8566-2008 RID A-2506-2009," Journal of Micro-Nanolithography Mems and Moems **8**, 043012-043012 (2009).
18. A. Ganjoo, H. Jain, C. Yu, J. Irudayaraj, and C. G. Pantano, "Detection and fingerprinting of pathogens: Mid-IR biosensor using amorphous chalcogenide films," Journal of Non-Crystalline Solids **354**, 2757-2762 (2008).
  19. N. Ho, M. C. Phillips, H. Qiao, P. J. Allen, K. Krishnaswami, B. J. Riley, T. L. Myers, and N. C. Anheier, "Single-mode low-loss chalcogenide glass waveguides for the mid-infrared," Opt. Lett. **31**, 1860-1862 (2006).
  20. R. G. DeCorby, N. Ponnampalam, M. M. Pai, H. T. Nguyen, P. K. Dwivedi, T. J. Clement, C. J. Haugen, J. N. McMullin, and S. O. Kasap, "High index contrast waveguides in chalcogenide glass and polymer," Ieee Journal of Selected Topics in Quantum Electronics **11**, 539-546 (2005).
  21. J. F. Viens, C. Meneghini, A. Villeneuve, T. V. Galstian, E. J. Knystautas, M. A. Duguay, K. A. Richardson, and T. Cardinal, "Fabrication and characterization of integrated optical waveguides in sulfide chalcogenide glasses RID A-6012-2011," Journal of Lightwave Technology **17**, 1184-1191 (1999).
  22. D.-Y. Choi, S. Madden, A. Rode, R. Wang, and B. Luther-Davies, "Fabrication of low loss Ge<sub>33</sub>As<sub>12</sub>Se<sub>55</sub> (AMTIR-1) planar waveguides RID A-4937-2008," Applied Physics Letters **91**, 011115-011115 (2007).
  23. Y. L. Ruan, W. T. Li, R. Jarvis, N. Madsen, A. Rode, and B. Luther-Davies, "Fabrication and characterization of low loss rib chalcogenide waveguides made by dry etching," Optics Express **12**, 5140-5145 (2004).
  24. X. Xia, Q. Chen, C. Tsay, C. B. Arnold, and C. K. Madsen, "Low-loss chalcogenide waveguides on lithium niobate for the mid-infrared," Opt. Lett. **35**, 3228-3230 (2010).
  25. J. Hu, V. Tarasov, N. Carlie, N.-N. Feng, L. Petit, A. Agarwal, K. Richardson, and L. Kimerling, "Si-CMOS-compatible lift-off fabrication of low-loss planar chalcogenide waveguides RID B-9534-2008 RID A-6012-2011," Optics Express **15**, 11798-11807 (2007).
  26. X. Gai, T. Han, A. Prasad, S. Madden, D.-Y. Choi, R. Wang, D. Bulla, and B. Luther-Davies, "Progress in optical waveguides fabricated from chalcogenide glasses RID A-4937-2008," Optics Express **18**, 26635-26646 (2010).
  27. G. B. Hoffman, W. Zhou, R. Sooryakumar, and R. M. Reano, "Direct write of optical waveguides on chalcogenide thin films using electron beams," Journal of Vacuum Science & Technology B **27**, 2737-2741 (2009).
  28. Y. Ruan, M.-K. Kim, Y.-H. Lee, B. Luther-Davies, and A. Rode, "Fabrication of high-Q chalcogenide photonic crystal resonators by e-beam lithography RID C-2015-2011," Applied Physics Letters **90**, 071102-071102 (2007).
  29. K. Suzuki, Y. Hamachi, and T. Baba, "Fabrication and characterization of chalcogenide glass photonic crystal waveguides," Optics Express **17**, 22393-22400 (2009).
  30. D. Freeman, S. Madden, and B. Luther-Davies, "Fabrication of planar photonic crystals in a chalcogenide glass using a focused ion beam," Optics Express **13**, 3079-3086 (2005).
  31. R. J. Martin-Palma, T. E. Clark, and C. G. Pantano, "Fabrication of two-dimensional photonic crystals in a chalcogenide glass," International Journal of Nanotechnology **6**, 1113-1120 (2009).
  32. T. Han, S. Madden, D. Bulla, and B. Luther-Davies, "Low loss Chalcogenide glass waveguides by thermal nano-imprint lithography," Optics Express **18**, 19286-19291 (2010).

33. Z. G. Man, W. Pan, D. Furniss, T. M. Benson, A. B. Seddon, T. Kohoutek, J. Orava, and T. Wagner, "Embossing of chalcogenide glasses: monomode rib optical waveguides in evaporated thin films RID D-1093-2011," *Opt. Lett.* **34**, 1234-1236 (2009).
34. W. J. Pan, D. Furniss, H. Rowe, C. A. Miller, A. Loni, P. Sewell, T. M. Benson, and A. B. Seddon, "Fine embossing of chalcogenide glasses: First time submicron definition of surface embossed features," *Journal of Non-Crystalline Solids* **353**, 1302-1306 (2007).
35. A. B. Seddon, W. J. Pan, D. Furniss, C. A. Miller, H. Rowe, D. Zhang, E. McBrearty, Y. Zhang, A. Loni, P. Sewell, and T. M. Benson, "Fine embossing of chalcogenide glasses - A new fabrication route for photonic integrated circuits," *Journal of Non-Crystalline Solids* **352**, 2515-2520 (2006).
36. T. Han, S. Madden, S. Debbarma, and B. Luther-Davies, "Improved method for hot embossing As<sub>2</sub>S<sub>3</sub> waveguides employing a thermally stable chalcogenide coating," *Optics Express* **19**, 25447-25453 (2011).
37. G. C. Chern and I. Lauks, "Spin-Coated Amorphous-Chalcogenide Films," *J. Appl. Phys.* **53**, 6979-6982 (1982).
38. E. Hajto, P. J. S. Ewen, R. Belford, J. Hajto, and A. E. Owen, "Optical-Properties of Spin-Coated Amorphous-Chalcogenide Thin-Films," *Journal of Non-Crystalline Solids* **97-8**, 1191-1194 (1987).
39. T. Wagner, T. Kohoutek, M. Vlcek, M. Munzar, and M. Frumar, "Spin-coated Ag<sub>x</sub>(As<sub>0.33</sub>S<sub>0.67</sub>)(100-x) films: preparation and structure," *Journal of Non-Crystalline Solids* **326**, 165-169 (2003).
40. X. M. Zhao, Y. N. Xia, and G. M. Whitesides, "Fabrication of three-dimensional microstructures: Microtransfer molding RID E-8499-2011," *Advanced Materials* **8**, 837-& (1996).
41. T. Barwicz and H. A. Haus, "Three-dimensional analysis of scattering losses due to sidewall roughness, in microphotonic waveguides," *Journal of Lightwave Technology* **23**, 2719-2732 (2005).
42. J. Hu, N.-N. Feng, N. Carlie, L. Petit, A. Agarwal, K. Richardson, and L. Kimerling, "Optical loss reduction in high-index-contrast chalcogenide glass waveguides via thermal reflow RID B-9534-2008 RID A-6012-2011," *Optics Express* **18**, 1469-1478 (2010).
43. C. J. Rowlands, L. Su, and S. R. Elliott, "Rapid Prototyping of Low-Loss IR Chalcogenide-Glass Waveguides by Controlled Remelting," *Chemphyschem* **11**, 2393-2398 (2010).
44. B. Temelkuran, S. D. Hart, G. Benoit, J. D. Joannopoulos, and Y. Fink, "Wavelength-scalable hollow optical fibres with large photonic bandgaps for CO<sub>2</sub> laser transmission," *Nature* **420**, 650-653 (2002).
45. Y. Yi, S. Akiyama, P. Bermel, X. Duan, and L. C. Kimerling, "Sharp bending of on-chip silicon Bragg cladding waveguide with light guiding in low index core materials," *Ieee Journal of Selected Topics in Quantum Electronics* **12**, 1345-1348 (2006).
46. Y. Yi, S. Akiyama, P. Bermel, X. M. Duan, and L. C. Kimerling, "On-chip Si-based Bragg cladding waveguide with high index contrast bilayers," *Optics Express* **12**, 4775-4780 (2004).
47. R. G. DeCorby, N. Ponnampalam, H. T. Nguyen, M. M. Pai, and T. J. Clement, "Guided self-assembly of integrated hollow Bragg waveguides," *Optics Express* **15**, 3902-3915 (2007).
48. N. Ponnampalam and R. G. DeCorby, "Self-assembled hollow waveguides with hybrid metal-dielectric Bragg claddings," *Optics Express* **15**, 12595-12604 (2007).
49. A. V. Kolobov and S. R. Elliott, "Photodoping of Amorphous Chalcogenides by Metals," *Advances in Physics* **40**, 625-684 (1991).

50. R. G. DeCorby, N. Ponnampalam, E. Epp, T. Allen, and J. N. McMullin, "Chip-scale spectrometry based on tapered hollow Bragg waveguides," *Optics Express* **17**, 16632-16645 (2009).
51. N. Ponnampalam and R. G. DeCorby, "Out-of-plane coupling at mode cutoff in tapered hollow waveguides with omnidirectional reflector claddings," *Optics Express* **16**, 2894-2908 (2008).
52. C. Tsay, F. Toor, C. F. Gmachl, and C. B. Arnold, "Chalcogenide glass waveguides integrated with quantum cascade lasers for on-chip mid-IR photonic circuits," *Opt. Lett.* **35**, 3324-3326 (2010).
53. V. Singh, J. Hu, T. Zens, J. Wang, P. T. Lin, J. Wilkinson, S. Novak, J. D. Musgraves, L. Kimerling, K. Richardson, and A. Agarwal, "Novel Designs for On-chip Mid-Infrared Detectors Integrated with Chalcogenide Waveguides," in *Integrated Photonics Research, Silicon and Nanophotonics*, (Toronto, Canada, 2011).
54. D. D. Nelson, J. H. Shorter, J. B. McManus, and M. S. Zahniser, "Sub-part-per-billion detection of nitric oxide in air using a thermoelectrically cooled mid-infrared quantum cascade laser spectrometer," *Applied Physics B-Lasers and Optics* **75**, 343-350 (2002).
55. G. N. Rao and A. Karpf, "External cavity tunable quantum cascade lasers and their applications to trace gas monitoring," *Applied Optics* **50**, A100-A115 (2011).
56. A. Ganjoo, H. Jain, C. Yu, R. Song, J. V. Ryan, J. Irudayaraj, Y. J. Ding, and C. G. Pantano, "Planar chalcogenide glass waveguides for IR evanescent wave sensors," *Journal of Non-Crystalline Solids* **352**, 584-588 (2006).
57. J. Hu, V. Tarasov, A. Agarwal, L. Kimerling, N. Carlie, L. Petit, and K. Richardson, "Fabrication and testing of planar chalcogenide waveguide integrated microfluidic sensor RID B-9534-2008 RID A-6012-2011," *Optics Express* **15**, 2307-2314 (2007).
58. A. Zakery, "Low loss waveguides in pulsed laser deposited arsenic sulfide chalcogenide films," *Journal of Physics D-Applied Physics* **35**, 2909-2913 (2002).
59. L. S. Rothman, I. E. Gordon, A. Barbe, D. C. Benner, P. E. Bernath, M. Birk, V. Boudon, L. R. Brown, A. Campargue, J. P. Champion, K. Chance, L. H. Coudert, V. Dana, V. M. Devi, S. Fally, J. M. Flaud, R. R. Gamache, A. Goldman, D. Jacquemart, I. Kleiner, N. Lacome, W. J. Lafferty, J. Y. Mandin, S. T. Massie, S. N. Mikhailenko, C. E. Miller, N. Moazzen-Ahmadi, O. V. Naumenko, A. V. Nikitin, J. Orphal, V. I. Perevalov, A. Perrin, A. Predoi-Cross, C. P. Rinsland, M. Rotger, M. Simeckova, M. A. H. Smith, K. Sung, S. A. Tashkun, J. Tennyson, R. A. Toth, A. C. Vandaele, and J. Vander Auwera, "The HITRAN 2008 molecular spectroscopic database RID B-6567-2012 RID A-4504-2010 RID C-3963-2009 RID A-7043-2008 RID A-8667-2012," *Journal of Quantitative Spectroscopy & Radiative Transfer* **110**, 533-572 (2009).
60. Z. Yang, M. K. Fah, K. A. Reynolds, J. D. Sexton, M. R. Riley, M.-L. Anne, B. Bureau, and P. Lucas, "Opto-electrophoretic detection of bio-molecules using conducting chalcogenide glass sensors," *Optics Express* **18**, 26754-26759 (2010).
61. M.-L. Anne, J. Keirsse, V. Nazabal, K. Hyodo, S. Inoue, C. Boussard-Pledel, H. Lhermite, J. Charrier, K. Yanakata, O. Loreal, J. Le Person, F. Colas, C. Compere, and B. Bureau, "Chalcogenide Glass Optical Waveguides for Infrared Biosensing," *Sensors* **9**, 7398-7411 (2009).
62. C. X. Yu, A. Ganjoo, H. Jain, C. G. Pantano, and J. Irudayaraj, "Mid-IR biosensor: Detection and fingerprinting of pathogens on gold island functionalized chalcogenide films," *Analytical Chemistry* **78**, 2500-2506 (2006).
63. H. K. Hunt, C. Soteropulos, and A. M. Armani, "Bioconjugation Strategies for Microtoroidal Optical Resonators RID A-8132-2010," *Sensors* **10**, 9317-9336 (2010).

64. J. T. Robinson, K. Preston, O. Painter, and M. Lipson, "First-principle derivation of gain in high-index-contrast waveguides RID B-1130-2009," *Optics Express* **16**, 16659-16669 (2008).
65. J. F. Bauters, M. J. R. Heck, D. John, D. Dai, M.-C. Tien, J. S. Barton, A. Leinse, R. G. Heideman, D. J. Blumenthal, and J. E. Bowers, "Ultra-low-loss high-aspect-ratio Si(3)N(4) waveguides RID F-4530-2011 RID H-1807-2011," *Optics Express* **19**, 3163-3174 (2011).
66. S. J. Madden, D. Y. Choi, D. A. Bulla, A. V. Rode, B. Luther-Davies, V. G. Ta'eed, M. D. Pelusi, and B. J. Eggleton, "Long, low loss etched As<sub>2</sub>S<sub>3</sub> chalcogenide waveguides for all-optical signal regeneration," *Optics Express* **15**, 14414-14421 (2007).
67. A. Densmore, M. Vachon, D. X. Xu, S. Janz, R. Ma, Y. H. Li, G. Lopinski, A. Delage, J. Lapointe, C. C. Luebbert, Q. Y. Liu, P. Cheben, and J. H. Schmid, "Silicon photonic wire biosensor array for multiplexed real-time and label-free molecular detection," *Opt. Lett.* **34**, 3598-3600 (2009).
68. L. Jiang and S. Pau, "Integrated waveguide with a microfluidic channel in spiral geometry for spectroscopic applications," *Applied Physics Letters* **90**, 111108-111108 (2007).
69. J. T. Robinson, L. Chen, and M. Lipson, "On-chip gas detection in silicon optical microcavities," *Optics Express* **16**, 4296-4301 (2008).
70. J. J. Hu, V. Tarasov, A. Agarwal, L. Kimerling, N. Carlie, L. Petit, and K. Richardson, "Fabrication and testing of planar chalcogenide waveguide integrated microfluidic sensor," *Optics Express* **15**, 2307-2314 (2007).
71. J. J. Hu, N. Carlie, N. N. Feng, L. Petit, A. Agarwal, K. Richardson, and L. Kimerling, "Planar waveguide-coupled, high-index-contrast, high-Q resonators in chalcogenide glass for sensing," *Opt. Lett.* **33**, 2500-2502 (2008).
72. N. Carlie, J. D. Musgraves, B. Zdyrko, I. Luzinov, J. Hu, V. Singh, A. Agarwal, L. C. Kimerling, A. Canciamilla, F. Morichetti, A. Melloni, and K. Richardson, "Integrated chalcogenide waveguide resonators for mid-IR sensing: leveraging material properties to meet fabrication challenges RID D-9260-2011 RID B-9534-2008 RID A-3735-2009 RID A-6012-2011," *Optics Express* **18**, 26728-26743 (2010).
73. J. Hu, N. Carlie, L. Petit, A. Agarwal, K. Richardson, and L. Kimerling, "Demonstration of chalcogenide glass racetrack microresonators RID B-9534-2008 RID A-6012-2011," *Opt. Lett.* **33**, 761-763 (2008).
74. M. E. Solmaz, D. B. Adams, W. C. Tan, W. T. Snider, and C. K. Madsen, "Vertically integrated As(2)S(3) ring resonator on LiNbO(3)," *Opt. Lett.* **34**, 1735-1737 (2009).
75. M. W. Lee, C. Grillet, C. Monat, E. Maegi, S. Tomljenovic-Hanic, X. Gai, S. Madden, D.-Y. Choi, D. Bulla, B. Luther-Davies, and B. J. Eggleton, "Photosensitive and thermal nonlinear effects in chalcogenide photonic crystal cavities," *Optics Express* **18**, 26695-26703 (2010).
76. M. W. Lee, C. Grillet, S. Tomljenovic-Hanic, E. C. Maegi, D. J. Moss, B. J. Eggleton, X. Gai, S. Madden, D.-Y. Choi, D. A. P. Bulla, and B. Luther-Davies, "Photowritten high-Q cavities in two-dimensional chalcogenide glass photonic crystals RID B-8721-2011," *Opt. Lett.* **34**, 3671-3673 (2009).
77. A. Yariv, "Universal relations for coupling of optical power between microresonators and dielectric waveguides," *Electronics Letters* **36**, 321-322 (2000).
78. R. W. Boyd and J. E. Heebner, "Sensitive disk resonator photonic biosensor RID C-2411-2009," *Applied Optics* **40**, 5742-5747 (2001).
79. J. Hu, N. Carlie, L. Petit, A. Agarwal, K. Richardson, and L. C. Kimerling, "Cavity-Enhanced IR Absorption in Planar Chalcogenide Glass Microdisk Resonators:

- Experiment and Analysis RID B-9534-2008 RID A-6012-2011," *Journal of Lightwave Technology* **27**, 5240-5245 (2009).
80. A. Nitkowski, A. Baeumner, and M. Lipson, "On-chip spectrophotometry for bioanalysis using microring resonators," *Biomedical Optics Express* **2**, 271-277 (2011).
  81. S. Shaji, S. M. Eappen, T. M. A. Rasheed, and K. P. R. Nair, "NIR vibrational overtone spectra of N-methylaniline, N,N-dimethylaniline and N,N-diethylaniline - a conformational structural analysis using local mode model," *Spectrochimica Acta Part A-Molecular and Biomolecular Spectroscopy* **60**, 351-355 (2004).
  82. A. Nitkowski, L. Chen, and M. Lipson, "Cavity-enhanced on-chip absorption spectroscopy using microring resonators," *Optics Express* **16**, 11930-11936 (2008).
  83. G. Gibson, S. D. Monk, and M. Padgett, "A field-portable, laser-diode spectrometer for the ultra-sensitive detection of hydrocarbon gases," *Journal of Modern Optics* **49**, 769-776 (2002).
  84. T. McGarvey, A. Conjusteau, and H. Mabuchi, "Finesse and sensitivity gain in cavity-enhanced absorption spectroscopy of biomolecules in solution," *Optics Express* **14**, 10441-10451 (2006).
  85. J. Hu, "Ultra-sensitive chemical vapor detection using micro-cavity photothermal spectroscopy," *Optics Express* **18**, 22174-22186 (2010).
  86. H. Lin, Y. Zou, and J. Hu, "Double resonance 1-D photonic crystal cavities for single-molecule mid-infrared photothermal spectroscopy: theory and design," *Opt. Lett.* **37**, 1304-1206 (2012).
  87. J. N. Anker, W. P. Hall, O. Lyandres, N. C. Shah, J. Zhao, and R. P. Van Duyne, "Biosensing with plasmonic nanosensors," *Nature Materials* **7**, 442-453 (2008).
  88. J. Homola, "Present and future of surface plasmon resonance biosensors," *Anal. Bioanal. Chem.* **377**, 528-539 (2003).
  89. J. Homola, "Surface plasmon resonance sensors for detection of chemical and biological species," *Chemical reviews* **108**, 462-493 (2008).
  90. J. Homola, S. S. Yee, and G. Gauglitz, "Surface plasmon resonance sensors: review," *Sensors and Actuators B-Chemical* **54**, 3-15 (1999).
  91. B. Liedberg, C. Nylander, and I. Lundstrom, "Biosensing with Surface-Plasmon Resonance - how it all Started," *Biosensors & bioelectronics* **10**, R1-R9 (1995).
  92. P. S. Katsamba, I. Navratilova, M. Calderon-Cacia, L. Fan, K. Thornton, M. D. Zhu, T. Vanden Bos, C. Forte, D. Friend, I. Laird-Offringa, G. Tavares, J. Whatley, E. G. Shi, A. Widom, K. C. Lindquist, S. Klakamp, A. Drake, D. Bohmann, M. Roell, L. Rose, J. Dorocke, B. Roth, B. Luginbuhl, and D. G. Myszka, "Kinetic analysis of a high-affinity antibody/antigen interaction performed by multiple Biacore users," *Analytical Biochemistry* **352**, 208-221 (2006).
  93. W. Huber and F. Mueller, "Biomolecular interaction analysis in drug discovery using surface plasmon resonance technology," *Current pharmaceutical design* **12**, 3999-4021 (2006).
  94. R. Jha and A. K. Sharma, "Chalcogenide glass prism based SPR sensor with Ag-Au bimetallic nanoparticle alloy in infrared wavelength region," *Journal of Optics A-Pure and Applied Optics* **11**, 045502-045502 (2009).
  95. J. Le Person, F. Colas, C. Compere, M. Lehaitre, M. L. Anne, C. Bousard-Pledel, B. Bureau, J. L. Adam, S. Deputier, and M. Guilloux-Viry, "Surface plasmon resonance in chalcogenide glass-based optical system," *Sensors and Actuators B-Chemical* **130**, 771-776 (2008).

96. A. K. Sharma and R. Jha, "Surface plasmon resonance-based gas sensor with chalcogenide glass and bimetallic alloy nanoparticle layer," *J. Appl. Phys.* **106**, 103101-103101 (2009).
97. A. K. Sharma, R. Jha, and H. S. Pattanaik, "Design considerations for surface plasmon resonance based detection of human blood group in near infrared," *J. Appl. Phys.* **107**, 034701-034701 (2010).
98. F. Vollmer and S. Arnold, "Whispering-gallery-mode biosensing: label-free detection down to single molecules," *Nature Methods* **5**, 591-596 (2008).
99. F. Vollmer, D. Braun, A. Libchaber, M. Khoshshima, I. Teraoka, and S. Arnold, "Protein detection by optical shift of a resonant microcavity," *Applied Physics Letters* **80**, 4057-4059 (2002).
100. I. M. White, H. Oveys, and X. D. Fan, "Liquid-core optical ring-resonator sensors," *Opt. Lett.* **31**, 1319-1321 (2006).
101. M. Iqbal, M. A. Gleeson, B. Spaugh, F. Tybor, W. G. Gunn, M. Hochberg, T. Baehr-Jones, R. C. Bailey, and L. C. Gunn, "Label-Free Biosensor Arrays Based on Silicon Ring Resonators and High-Speed Optical Scanning Instrumentation," *Ieee Journal of Selected Topics in Quantum Electronics* **16**, 654-661 (2010).
102. M. Lee and P. M. Fauchet, "Two-dimensional silicon photonic crystal based biosensing platform for protein detection," *Optics Express* **15**, 4530-4535 (2007).
103. D. X. Xu, M. Vachon, A. Densmore, R. Ma, S. Janz, A. Delage, J. Lapointe, P. Cheben, J. H. Schmid, E. Post, S. Messaoudene, and J.-M. Fedeli, "Real-time cancellation of temperature induced resonance shifts in SOI wire waveguide ring resonator label-free biosensor arrays," *Optics Express* **18**, 22867-22879 (2010).
104. A. Yalcin, K. C. Papat, J. C. Aldridge, T. A. Desai, J. Hryniewicz, N. Chbouki, B. E. Little, O. King, V. Van, S. Chu, D. Gill, M. Anthes-Washburn, and M. S. Unlu, "Optical sensing of biomolecules using microring resonators RID A-9582-2009," *Ieee Journal of Selected Topics in Quantum Electronics* **12**, 148-155 (2006).
105. C. Y. Chao, W. Fung, and L. J. Guo, "Polymer microring resonators for biochemical sensing applications RID A-9100-2009," *Ieee Journal of Selected Topics in Quantum Electronics* **12**, 134-142 (2006).
106. C. Y. Chao and L. J. Guo, "Design and optimization of microring resonators in biochemical sensing applications RID A-9100-2009," *Journal of Lightwave Technology* **24**, 1395-1402 (2006).
107. J. Hu, N. Carlie, N.-N. Feng, L. Petit, A. Agarwal, K. Richardson, and L. Kimerling, "Planar waveguide-coupled, high-index-contrast, high-Q resonators in chalcogenide glass for sensing RID B-9534-2008 RID A-6012-2011," *Opt. Lett.* **33**, 2500-2502 (2008).
108. J. Giammarco, B. Zdyrko, L. Petit, J. D. Musgraves, J. Hu, A. Agarwal, L. Kimerling, K. Richardson, and I. Luginov, "Towards universal enrichment nanocoating for IR-ATR waveguides RID D-9260-2011 RID B-9534-2008 RID A-6012-2011," *Chemical Communications* **47**, 9104-9106 (2011).
109. K. Finsterbusch, N. J. Baker, V. G. Ta'eed, B. J. Eggleton, D.-Y. Choi, S. Madden, and B. Luther-Davies, "Higher-order mode grating devices in As<sub>2</sub>S<sub>3</sub> chalcogenide glass rib waveguides," *Journal of the Optical Society of America B-Optical Physics* **24**, 1283-1290 (2007).
110. L. Su, T. H. Lee, and S. R. Elliott, "Evanescent-wave excitation of surface-enhanced Raman scattering substrates by an optical-fiber taper," *Opt. Lett.* **34**, 2685-2687 (2009).
111. X. M. Qian and S. M. Nie, "Single-molecule and single-nanoparticle SERS: from fundamental mechanisms to biomedical applications RID E-4843-2011," *Chemical Society Reviews* **37**, 912-920 (2008).

112. P. L. Stiles, J. A. Dieringer, N. C. Shah, and R. R. Van Duyne, "Surface-Enhanced Raman Spectroscopy," *Annual Review of Analytical Chemistry* **1**, 601-626 (2008).
113. N. Felidj, J. Aubard, G. Levi, J. R. Krenn, A. Hohenau, G. Schider, A. Leitner, and F. R. Aussenegg, "Optimized surface-enhanced Raman scattering on gold nanoparticle arrays RID H-1257-2011," *Applied Physics Letters* **82**, 3095-3097 (2003).
114. C. J. Rowlands, L. Su, and S. R. Elliott, "Investigating the response of As(2)S(3)-based SERS substrates," *Optical Materials* **32**, 1413-1416 (2010).
115. L. Su, C. J. Rowlands, and S. R. Elliott, "Nanostructures fabricated in chalcogenide glass for use as surface-enhanced Raman scattering substrates," *Opt. Lett.* **34**, 1645-1647 (2009).
116. N. S. Kapany and R. J. Simms, "Recent developments in infrared fiber optics," *Infrared Physics* **5**, 69-& (1965).
117. J. D. Shephard, W. N. MacPherson, R. R. J. Maier, J. D. C. Jones, D. P. Hand, M. Mohebbi, A. K. George, P. J. Roberts, and J. C. Knight, "Single-mode mid-IR guidance in a hollow-core photonic crystal fiber," *Optics Express* **13**, 7139-7144 (2005).
118. T. D. Engeness, M. Ibanescu, S. G. Johnson, O. Weisberg, M. Skorobogatiy, S. Jacobs, and Y. Fink, "Dispersion tailoring and compensation by modal interactions in OmniGuide fibers," *Optics Express* **11**, 1175-1196 (2003).
119. J. Hu, C. R. Menyuk, L. B. Shaw, J. S. Sanghera, and I. D. Aggarwal, "Maximizing the bandwidth of supercontinuum generation in As(2)Se(3) chalcogenide fibers," *Optics Express* **18**, 6722-6739 (2010).
120. Z. Wang and N. Chocat, "Fiber-Optic Technologies in Laser-Based Therapeutics: Threads for a Cure," *Current Pharmaceutical Biotechnology* **11**, 384-397 (2010).
121. T. Ueda, K. Yamada, and T. Sugita, "MEASUREMENT OF GRINDING TEMPERATURE OF CERAMICS USING INFRARED RADIATION PYROMETER WITH OPTICAL FIBER," *Journal of Engineering for Industry-Transactions of the Asme* **114**, 317-322 (1992).
122. M. Saito, M. Takizawa, S. Sakuragi, and F. Tanei, "INFRARED IMAGE GUIDE WITH BUNDLED AS-S GLASS-FIBERS," *Applied Optics* **24**, 2304-2308 (1985).
123. J. Nishii, T. Yamashita, T. Yamagishi, C. Tanaka, and H. Stone, "Coherent infrared fiber image bundle," *Applied Physics Letters* **59**, 2639-2641 (1991).
124. M. Asobe, T. Ohara, I. Yokohama, and T. Kaino, "Low power all-optical switching in a nonlinear optical loop mirror using chalcogenide glass fibre," *Electronics Letters* **32**, 1396-1397 (1996).
125. R. E. Slusher, G. Lenz, J. Hodelin, J. Sanghera, L. B. Shaw, and I. D. Aggarwal, "Large Raman gain and nonlinear phase shifts in high-purity As<sub>2</sub>Se<sub>3</sub> chalcogenide fibers," *Journal of the Optical Society of America B-Optical Physics* **21**, 1146-1155 (2004).
126. O. S. Wolfbeis, "Fiber-optic chemical sensors and biosensors," *Analytical Chemistry* **78**, 3859-3873 (2006).
127. A. Leung, P. M. Shankar, and R. Mutharasan, "A review of fiber-optic biosensors," *Sensors and Actuators B-Chemical* **125**, 688-703 (2007).
128. M. E. Bosch, A. J. R. Sanchez, F. S. Rojas, and C. B. Ojeda, "Recent development in optical fiber biosensors," *Sensors* **7**, 797-859 (2007).
129. P. Rolfe, F. Scopesi, and G. Serra, "Advances in fibre-optic sensing in medicine and biology," *Measurement Science & Technology* **18**, 1683-1688 (2007).
130. M. Katz, A. Katzir, I. Schnitzer, and A. Bornstein, "QUANTITATIVE-EVALUATION OF CHALCOGENIDE GLASS-FIBER EVANESCENT-WAVE SPECTROSCOPY," *Applied Optics* **33**, 5888-5894 (1994).
131. A. Bornstein, M. Katz, A. Baram, and D. Wolfman, "Attenuated total reflection spectroscopy with chalcogenide bi-tapered fibers," *Proc. SPIE* **1591**, 256-262 (1991).

132. J. S. Sanghera, F. H. Kung, P. C. Pureza, V. Q. Nguyen, R. E. Miklos, and I. D. Aggarwal, "INFRARED EVANESCENT-ABSORPTION SPECTROSCOPY WITH CHALCOGENIDE GLASS-FIBERS," *Applied Optics* **33**, 6315-6322 (1994).
133. B. Bureau, X. H. Zhang, F. Smektala, J. L. Adam, J. Troles, H. L. Ma, C. Boussard-Pledel, J. Lucas, P. Lucas, D. Le Coq, M. R. Riley, and J. H. Simmons, "Recent advances in chalcogenide glasses," *Journal of Non-Crystalline Solids* **345**, 276-283 (2004).
134. A. Messica, A. Greenstein, and A. Katzir, "Theory of fiber-optic, evanescent-wave spectroscopy and sensors," *Applied Optics* **35**, 2274-2284 (1996).
135. D. Le Coq, K. Michel, G. Fonteneau, S. Hocde, C. Boussard-Pledel, and J. Lucas, "Infrared chalcogen glasses: chemical polishing and fibre remote spectroscopy," *International Journal of Inorganic Materials* **3**, 233-239 (2001).
136. S. Hocde, O. Loreal, O. Sire, C. Boussard-Pledel, B. Bureau, B. Turlin, J. Keirsse, P. Leroyer, and J. Lucas, "Metabolic imaging of tissues by infrared fiber-optic spectroscopy: an efficient tool for medical diagnosis," *Journal of Biomedical Optics* **9**, 404-407 (2004).
137. E. Lepine, Z. Y. Yang, Y. Gueguen, J. Troles, X. H. Zhang, B. Bureau, C. Boussard-Pledel, J. C. Sangleboeuf, and P. Lucas, "Optical microfabrication of tapers in low-loss chalcogenide fibers," *Journal of the Optical Society of America B-Optical Physics* **27**, 966-971 (2010).
138. M. F. Churbanov, G. E. Snopatin, V. S. Shiryaev, V. G. Plotnichenko, and E. M. Dianov, "Recent advances in preparation of high-purity glasses based on arsenic chalcogenides for fiber optics," *Journal of Non-Crystalline Solids* **357**, 2352-2357 (2011).
139. D. J. McEnroe and W. C. Lacourse, "TENSILE STRENGTHS OF SE, AS<sub>2</sub>S<sub>3</sub>, AS<sub>2</sub>SE<sub>3</sub>, AND GE<sub>30</sub>AS<sub>15</sub>SE<sub>55</sub> GLAS FIBERS," *Journal of the American Ceramic Society* **72**, 1491-1494 (1989).
140. E. M. Dianov, V. G. Plotnichenko, G. G. Devyatykh, M. F. Churbanov, and I. V. Scripachev, "MIDDLE-INFRARED CHALCOGENIDE GLASS-FIBERS WITH LOSSES LOWER THAN 100 DB KM<sup>-1</sup>," *Infrared Physics* **29**, 303-307 (1989).
141. C. T. Hach, K. CerquaRichardson, J. R. Varner, and W. C. LaCourse, "Density and microhardness of As-Se glasses and glass fibers," *Journal of Non-Crystalline Solids* **209**, 159-165 (1997).
142. S. H. Shieh and W. C. Lacourse, "A STUDY OF HIGH-STRENGTH ARSENIC TRISELENIDE GLASS-FIBERS," *Materials Chemistry and Physics* **35**, 21-27 (1993).
143. G. E. Snopatin, V. S. Shiryaev, V. G. Plotnichenko, E. M. Dianov, and M. F. Churbanov, "High-purity chalcogenide glasses for fiber optics," *Inorganic Materials* **45**, 1439-1460 (2009).
144. V. S. Shiryaev, J. L. Adam, X. H. Zhang, C. Boussard-Pledel, J. Lucas, and M. F. Churbanov, "Infrared fibers based on Te-As-Se glass system with low optical losses," *Journal of Non-Crystalline Solids* **336**, 113-119 (2004).
145. J. Sanghera and I. D. Aggarwal, "Drawing of chalcogenide glass optical fibres," in *Properties, Processing and Applications of Glass and Rare-Earth Doped Glasses for Optical Fibres*, D. Hewak, ed. (EMIS Datareviews Series, 1998), pp. 344-347.
146. J. Nishii, T. Yamashita, and T. Yamagishi, "CHALCOGENIDE GLASS-FIBER WITH A CORE CLADDING STRUCTURE," *Applied Optics* **28**, 5122-5127 (1989).
147. B. Bureau, S. Mauriceon, F. Charpentier, J. L. Adam, C. Boussard-Pledel, and X. H. Zhang, "Chalcogenide Glass Fibers for Infrared Sensing and Space Optics," *Fiber and Integrated Optics* **28**, 65-80 (2009).

148. T. Kanamori, Y. Terunuma, S. Takahashi, and T. Miyashita, "CHALCOGENIDE GLASS-FIBERS FOR MID-INFRARED TRANSMISSION," *Journal of Lightwave Technology* **2**, 607-613 (1984).
149. J. Nishii, S. Morimoto, I. Inagawa, R. Iizuka, T. Yamashita, and T. Yamagishi, "RECENT ADVANCES AND TRENDS IN CHALCOGENIDE GLASS-FIBER TECHNOLOGY - A REVIEW," *Journal of Non-Crystalline Solids* **140**, 199-208 (1992).
150. D. Le Coq, C. Boussard-Pledel, G. Fonteneau, T. Pain, B. Bureau, and J. L. Adam, "Chalcogenide double index fibers: fabrication, design, and application as a chemical sensor," *Materials Research Bulletin* **38**, 1745-1754 (2003).
151. D. Le Coq, C. Boussard-Pledel, G. Fonteneau, T. Pain, B. Bureau, and J. L. Adam, "A new approach of preform fabrication for chalcogenide fibers," *Journal of Non-Crystalline Solids* **326**, 451-454 (2003).
152. S. D. Savage, C. A. Miller, D. Furniss, and A. B. Seddon, "Extrusion of chalcogenide glass preforms and drawing to multimode optical fibers," *Journal of Non-Crystalline Solids* **354**, 3418-3427 (2008).
153. J. J. Kaufman, G. M. Tao, S. Shabahang, D. S. S. Deng, Y. Fink, and A. F. Abouraddy, "Thermal Drawing of High-Density Macroscopic Arrays of Well-Ordered Sub-5-nm-Diameter Nanowires," *Nano Letters* **11**, 4768-4773 (2011).
154. J. Troles, L. Brilland, F. Smektala, P. Houizot, F. Desevedavy, Q. Coulombier, N. Traynor, T. Chartier, T. N. Nguyen, J. L. Adam, and G. Renversez, "Chalcogenide Microstructured Fibers for Infrared Systems, Elaboration Modelization, and Characterization," *Fiber and Integrated Optics* **28**, 11-26 (2009).
155. T. M. Monro, D. J. Richardson, and P. J. Bennett, "Developing holey fibres for evanescent field devices," *Electronics Letters* **35**, 1188-1189 (1999).
156. M. El-Amraoui, G. Gadret, J. C. Jules, J. Fatome, C. Fortier, F. Desevedavy, I. Skripatchev, Y. Messaddeq, J. Troles, L. Brilland, W. Gao, T. Suzuki, Y. Ohishi, and F. Smektala, "Microstructured chalcogenide optical fibers from As<sub>2</sub>S<sub>3</sub> glass: towards new IR broadband sources," *Optics Express* **18**, 26655-26665 (2010).
157. D. A. C. Compton, S. L. Hill, N. A. Wright, M. A. Druy, J. Piche, W. A. Stevenson, and D. W. Vidrine, "INSITU FT-IR ANALYSIS OF A COMPOSITE CURING REACTION USING A MID-INFRARED TRANSMITTING OPTICAL FIBER," *Applied Spectroscopy* **42**, 972-979 (1988).
158. J. Heo, M. Rodrigues, S. J. Saggese, and G. H. Sigel, "REMOTE FIBEROPTIC CHEMICAL SENSING USING EVANESCENT-WAVE INTERACTIONS IN CHALCOGENIDE GLASS-FIBERS," *Applied Optics* **30**, 3944-3951 (1991).
159. J. S. Sanghera, F. H. Kung, L. E. Busse, P. C. Pureza, and I. D. Aggarwal, "INFRARED EVANESCENT ABSORPTION-SPECTROSCOPY OF TOXIC-CHEMICALS USING CHALCOGENIDE GLASS FIBERS," *Journal of the American Ceramic Society* **78**, 2198-2202 (1995).
160. M. L. Anne, E. L. La Salle, B. Bureau, J. Tristant, F. Brochot, C. Boussard-Pledel, H. L. Ma, X. H. Zhang, and J. L. Adam, "Polymerisation of an industrial resin monitored by infrared fiber evanescent wave spectroscopy," *Sensors and Actuators B-Chemical* **137**, 687-691 (2009).
161. K. Li and J. Meichsner, "In situ infrared fibre evanescent wave spectroscopy as a diagnostic tool for plasma polymerization in a gas discharge (vol 34, pg 1318, 2001)," *Journal of Physics D-Applied Physics* **34**, 1744-1744 (2001).
162. D. Le Coq, K. Michel, J. Keirsse, C. Boussard-Pledel, G. Fonteneau, B. Bureau, J. M. Le Quere, O. Sire, and J. Lucas, "Infrared glass fibers for in-situ sensing, chemical and biochemical reactions," *Comptes Rendus Chimie* **5**, 907-913 (2002).

163. J. Sanghera, L. B. Shaw, L. E. Busse, D. Talley, and I. D. Aggarwal, "Infrared transmitting fiber optics for biomedical applications," *Proc. SPIE* **3596**, 178-187 (1999).
164. K. Taga, B. Mizaikoff, and R. Kellner, "FIBER OPTIC EVANESCENT FIELD SENSORS FOR GASEOUS SPECIES USING MIR TRANSPARENT FIBERS," *Fresenius Journal of Analytical Chemistry* **348**, 556-559 (1994).
165. F. Charpentier, J. Troles, Q. Coulombier, L. Brilland, P. Houizot, F. Smektala, C. Boussard-Pledel, V. Nazabal, N. Thibaud, K. Le Pierres, Renversez, and B. Bureau, "CO(2) Detection Using Microstructured Chalcogenide Fibers," *Sensor Letters* **7**, 745-749 (2009).
166. W. J. Yoo, J. K. Seo, D. H. Cho, K. W. Jang, J. Heo, S.-C. Chung, B. Lee, B. G. Park, J. H. Moon, and S. Kim, "Chalcogenide optical fiber based sensor for non-invasive monitoring of respiration," *IEEE Symposium of Industrial Electronics & Applications* **2**, 617-619 (2009).
167. J. S. Sanghera, L. B. Shaw, L. E. Busse, V. Q. Nguyen, P. C. Pureza, B. C. Cole, B. B. Harbison, I. D. Aggarwal, R. Mossadegh, F. Kung, D. Talley, D. Roselle, and R. Miklos, "Development and infrared applications of chalcogenide glass optical fibers," *Fiber and Integrated Optics* **19**, 251-274 (2000).
168. K. Michel, B. Bureau, C. Boussard-Pledel, T. Jouan, J. L. Adam, K. Staubmann, and T. Baumann, "Monitoring of pollutant in waste water by infrared spectroscopy using chalcogenide glass optical fibers," *Sensors and Actuators B-Chemical* **101**, 252-259 (2004).
169. J. Keirsse, C. Boussard-Pledel, O. Loreal, O. Sire, B. Bureau, B. Turlin, P. Leroyer, and J. Lucas, "Chalcogenide glass fibers used as biosensors," *Journal of Non-Crystalline Solids* **326**, 430-433 (2003).
170. M. L. Anne, C. Le Lan, V. Monbet, C. Boussard-Pledel, M. Ropert, O. Sire, M. Pouchard, C. Jard, J. Lucas, J. L. Adam, P. Brissot, B. Bureau, and O. Loreal, "Fiber evanescent wave spectroscopy using the mid-infrared provides useful fingerprints for metabolic profiling in humans," *Journal of Biomedical Optics* **14**(2009).
171. T. Uemura, K. Nishida, M. Sakakida, K. Ichinose, S. Shimoda, and M. Shichiri, "Non-invasive blood glucose measurement by Fourier transform infrared spectroscopic analysis through the mucous membrane of the lip: application of a chalcogenide optical fiber system," *Front. Med. Biol. Eng.* **9**, 137-153 (1999).
172. J. Keirsse, C. Boussard-Pledel, O. Loreal, O. Sire, B. Bureau, P. Leroyer, B. Turlin, and J. Lucas, "IR optical fiber sensor for biomedical applications," *Vibrational Spectroscopy* **32**, 23-32 (2003).
173. J. Keirsse, E. Lahaye, A. Bouter, V. Dupont, C. Boussard-Pledel, B. Bureau, J. L. Adam, V. Monbet, and O. Sire, "Mapping bacterial surface population physiology in real-time: Infrared spectroscopy of *Proteus mirabilis* swarm colonies," *Applied Spectroscopy* **60**, 584-591 (2006).
174. P. Lucas, D. Le Coq, C. Juncker, J. Collier, D. E. Boesewetter, C. Boussard-Pledel, B. Bureau, and M. R. Riley, "Evaluation of toxic agent effects on lung cells by fiber evanescent wave spectroscopy," *Applied Spectroscopy* **59**, 1-9 (2005).
175. P. Houizot, C. Boussard-Pledel, A. J. Faber, L. K. Cheng, B. Bureau, P. A. Van Nijnatten, W. L. M. Gielesen, J. P. do Carmo, and J. Lucas, "Infrared single mode chalcogenide glass fiber for space," *Optics Express* **15**, 12529-12538 (2007).
176. S. Danto, P. Houizot, C. Boussard-Pledel, X. H. Zhang, F. Smektala, and J. Lucas, "A family of far-infrared-transmitting glasses in the Ga-Ge-Te system for space applications," *Advanced Functional Materials* **16**, 1847-1852 (2006).

177. A. A. Wilhelm, C. Boussard-Pledel, Q. Coulombier, J. Lucas, B. Bureau, and P. Lucas, "Development of far-infrared-transmitting te based glasses suitable for carbon dioxide detection and space optics," *Advanced Materials* **19**, 3796-+ (2007).
178. S. Mauriceon, B. Bureau, C. Boussard-Pledel, A. J. Faber, P. Lucas, X. H. Zhang, and J. Lucas, "Selenium modified GeTe(4) based glasses optical fibers for far-infrared sensing," *Optical Materials* **33**, 660-663 (2011).
179. S. Miclos and T. Zisu, "Chalcogenide fibre displacement sensor," *Journal of Optoelectronics and Advanced Materials* **3**, 373-376 (2001).
180. A. F. Abouraddy, M. Bayindir, G. Benoit, S. D. Hart, K. Kuriki, N. Orf, O. Shapira, F. Sorin, B. Temelkuran, and Y. Fink, "Towards multimaterial multifunctional fibres that see, hear, sense and communicate," *Nature Materials* **6**, 336-347 (2007).
181. S. Egusa, Z. Wang, N. Chocat, Z. M. Ruff, A. M. Stolyarov, D. Shemuly, F. Sorin, P. T. Rakich, J. D. Joannopoulos, and Y. Fink, "Multimaterial piezoelectric fibres," *Nature Materials* **9**, 643-648 (2010).
182. A. F. Abouraddy, O. Shapira, M. Bayindir, J. Arnold, F. Sorin, D. S. Hinczewski, J. D. Joannopoulos, and Y. Fink, "Large-scale optical-field measurements with geometric fibre constructs," *Nature Materials* **5**, 532-536 (2006).
183. S. Danto, Z. Ruff, Z. Wang, J. D. Joannopoulos, and Y. Fink, "Ovonic Memory Switching in Multimaterial Fibers," *Advanced Functional Materials* **21**, 1095-1101 (2011).
184. S. Danto, F. Sorin, N. D. Orf, Z. Wang, S. A. Speakman, J. D. Joannopoulos, and Y. Fink, "Fiber Field-Effect Device Via In Situ Channel Crystallization," *Advanced Materials* **22**, 4162-+ (2010).
185. R. J. Anderson, D. J. Bendell, and P. W. Groundwater, *Organic Spectroscopic Analysis* (2004).
186. C. T. Moynihan, P. B. Macedo, M. S. Maklad, R. K. Mohr, and R. E. Howard, "INTRINSIC AND IMPURITY INFRARED-ABSORPTION IN AS<sub>2</sub>SE<sub>3</sub> GLASS," *Journal of Non-Crystalline Solids* **17**, 369-385 (1975).
187. J. T. Gopinath, M. Soljagic, E. P. Ippen, V. N. Fuflyigin, W. A. King, and M. Shurgalin, "Third order nonlinearities in Ge-As-Se-based glasses for telecommunications applications," *J. Appl. Phys.* **96**, 6931-6933 (2004).
188. J. D. Musgraves, N. Carlie, J. Hu, L. Petit, A. Agarwal, L. C. Kimerling, and K. A. Richardson, "Comparison of the optical, thermal and structural properties of Ge-Sb-S thin films deposited using thermal evaporation and pulsed laser deposition techniques," *Acta Mater.* **59**, 5032-5039 (2011).
189. "Infrared Chalcogenide Glasses IG2, IG3, IG4, IG5, and IG6," (Schott North America, Durea, PA, 2009).
190. H. A. Qiao, N. C. Anheier, J. D. Musgraves, K. Richardson, and D. Hewak, "Measurement of Chalcogenide Glass Optical Dispersion Using a Mid-Infrared Prism Coupler," in *SPIE Defense Security and Sensing 2011*, (Orlando, FL, 2011).
191. B. J. Frey, D. B. Leviton, and T. J. Madison, "Temperature dependent refractive index of silicon and germanium," (2006).
192. P. J. Webber and J. A. Savage, "SOME PHYSICAL-PROPERTIES OF GE-AS-SE INFRARED OPTICAL GLASSES," *Journal of Non-Crystalline Solids* **20**, 271-283 (1976).
193. J. D. Musgraves, P. Wachtel, S. Novak, J. Wilkinson, and K. Richardson, "Composition dependence of the viscosity and other physical properties in the arsenic selenide glass system," *J. Appl. Phys.* **110**, 63503-63503 (2011).
194. J. J. Hu, N. N. Feng, N. Carlie, L. Petit, A. Agarwal, K. Richardson, and L. Kimerling, "Optical loss reduction in high-index-contrast chalcogenide glass waveguides via thermal reflow," *Optics Express* **18**, 1469-1478 (2010).

195. N. Carlie, J. D. Musgraves, B. Zdyrko, I. Luzinov, J. J. Hu, V. Singh, A. Agarwal, L. C. Kimerling, A. Canciamilla, F. Morichetti, A. Melloni, and K. Richardson, "Integrated chalcogenide waveguide resonators for mid-IR sensing: leveraging material properties to meet fabrication challenges," *Optics Express* **18**, 26728-26743 (2010).